



1 Foehn Winds at Pine Island Glacier and their role in Ice Changes

2
3 Diana Francis^{1*}, Ricardo Fonseca¹, Kyle S. Mattingly², Stef Lhermitte^{3,5}, Catherine
4 Walker⁴

5
6 ¹ The Environmental and Geophysical Sciences (ENGEOS) Lab, Khalifa University, P. O. Box
7 127788, Abu Dhabi, United Arab Emirates.

8 ² Space Science and Engineering Center, University of Wisconsin-Madison, Madison, WI, USA.

9 ³ Department of Earth & Environmental Sciences, KU Leuven, Belgium.

10 ⁴ Department of Applied Ocean Physics and Engineering, Woods Hole Oceanographic
11 Institution, Woods Hole, MA, USA.

12 ⁵ Department of Geosciences & Remote Sensing, Delft University of Technology, Netherlands.

13
14 *Corresponding author: diana.francis@ku.ac.ae

15 Abstract

16 Pine Island Glacier (PIG) has recently experienced increased ice loss mostly attributed to basal
17 melt and ocean-ice dynamics. However, atmospheric forcing also plays a role in the ice mass
18 budget, as besides lower-latitude warm air intrusions, the steeply sloping terrain that surrounds the
19 glacier promotes frequent Foehn winds. An investigation of 41-years of reanalysis data reveals
20 that Foehn occurs more frequently from June to October, with Foehn episodes typically lasting
21 about 5 to 9h. An analysis of the surface mass balance indicated that their largest impact is on the
22 surface sublimation, which is increased by about 1.4 mm water equivalent (w.e.) day⁻¹ with respect
23 to no-Foehn events. Blowing snow makes roughly the same contribution as snowfall, around 0.34-
24 0.36 mm w.e. day⁻¹, but with the opposite sign. The melting rate is three orders of magnitude smaller
25 than the surface sublimation rate. The negative phase of the Antarctic Oscillation and the positive
26 phase of the Southern Annular Mode promote the occurrence of Foehn at PIG. A particularly
27 strong event took place on 09-11 November 2011, when 10-m winds speeds in excess of 20 m s⁻¹
28 led to downward sensible heat fluxes higher than 75 W m⁻² as they descended the mountainous
29 terrain. Surface sublimation and blowing snow sublimation dominated the surface mass balance,
30 with magnitudes of up to 0.13 mm w.e. hr⁻¹. Satellite data indicated an hourly surface melting area
31 exceeding 100 km². Our results stress the importance of the atmospheric forcing on the ice mass
32 balance at PIG.

33 **Keywords:** Pine Island Glacier, Foehn Winds, Amundsen Sea Low, Snow Sublimation, Surface
34 Mass Balance, Ice Loss.

35

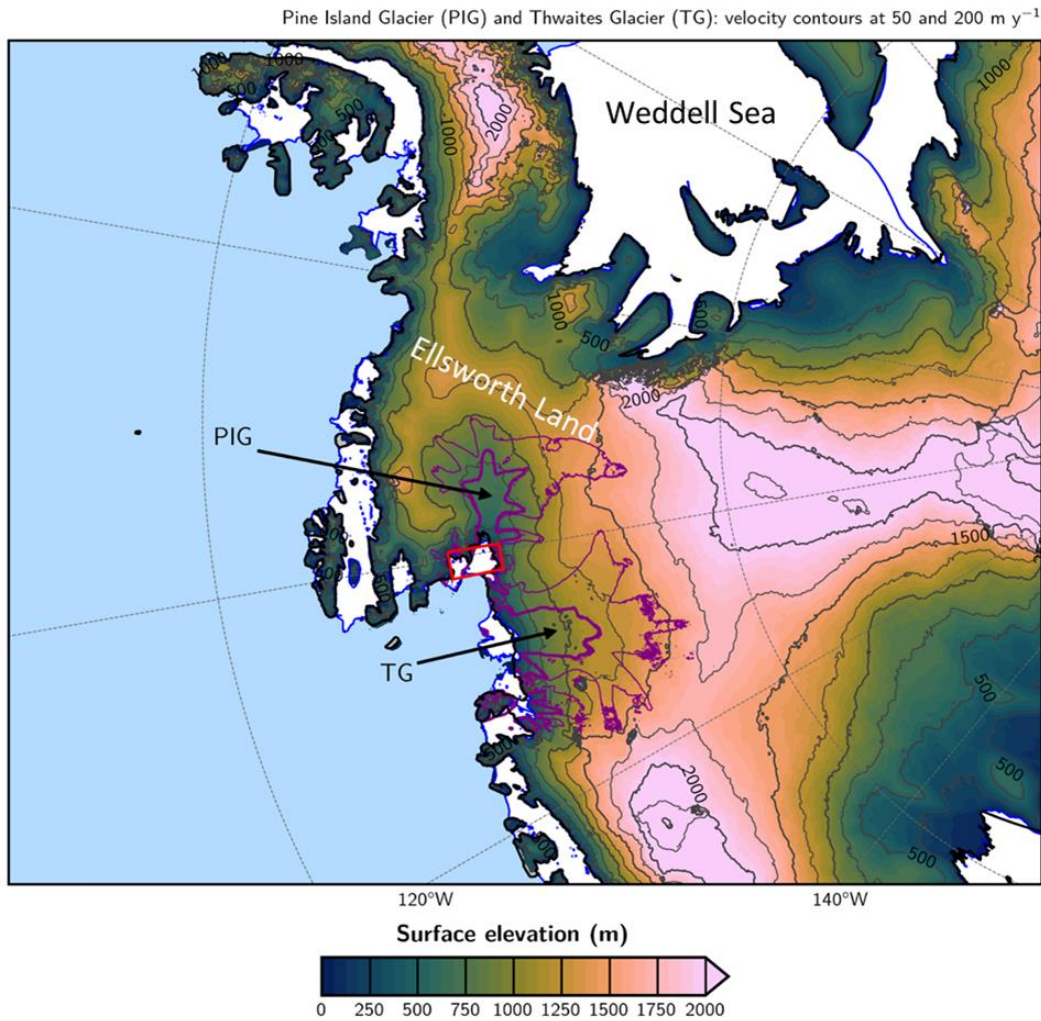


36 1. Introduction

37 The West Antarctic Ice Sheet and its marine terminating ice shelves have been thinning rapidly
38 in the last few decades, contributing to roughly 10% of the observed global mean sea-level rise
39 (Jenkins et al., 2010; Smith et al., 2020). A collapse of the West Antarctic Ice Sheet alone is
40 estimated to lead to a 3 m rise in the global sea-level (Bamber et al., 2009b), and model simulations
41 suggest it can be initiated by an ocean warming of approximately 1.2°C (Rosier et al., 2021). One
42 of the main contributors to the ice loss in West Antarctica is Pine Island Glacier (PIG), Fig. 1a,
43 which is presently Antarctica's single largest contributor to sea-level rise (Favier et al., 2014;
44 Joughin et al., 2021; Lhermitte et al., 2021). Over the last two decades PIG has lost more than a
45 trillion tons of ice, which corresponds to a roughly 3 mm rise in sea-level (De Rydt et al., 2021).
46 Satellite images indicate a jump in the average volume loss rate around PIG from roughly 2.6 km³
47 y⁻¹ in 1995 to 10.1 km³ y⁻¹ in 2006 (Wingham et al., 2009), with recent studies stressing a further
48 speedup of ice loss since 2017 (Joughin et al., 2021; Lhermitte et al., 2021; Nilsson et al., 2022).
49 In fact, Li et al. (2022) reported a decrease in elevation around PIG, as estimated from satellite
50 measurements, at a rate of approximately $-2 \pm 0.04 \text{ m y}^{-1}$ from 2016 to 2019. Satellite data indicates
51 an ice velocity magnitude in excess of 200 m y⁻¹ over a broad region, Fig. 1a, with peak values
52 higher than 4.5 km y⁻¹ (Liu et al., 2022). The ice loss at PIG can be seen by the rapid retreat of the
53 ice front, Fig. 1b, in particular since 2015, with major calving events taking place in October-
54 November 2018 and February 2020 (Liu et al., 2022; Lhermitte et al., 2021).

55
56

(a)



(b)

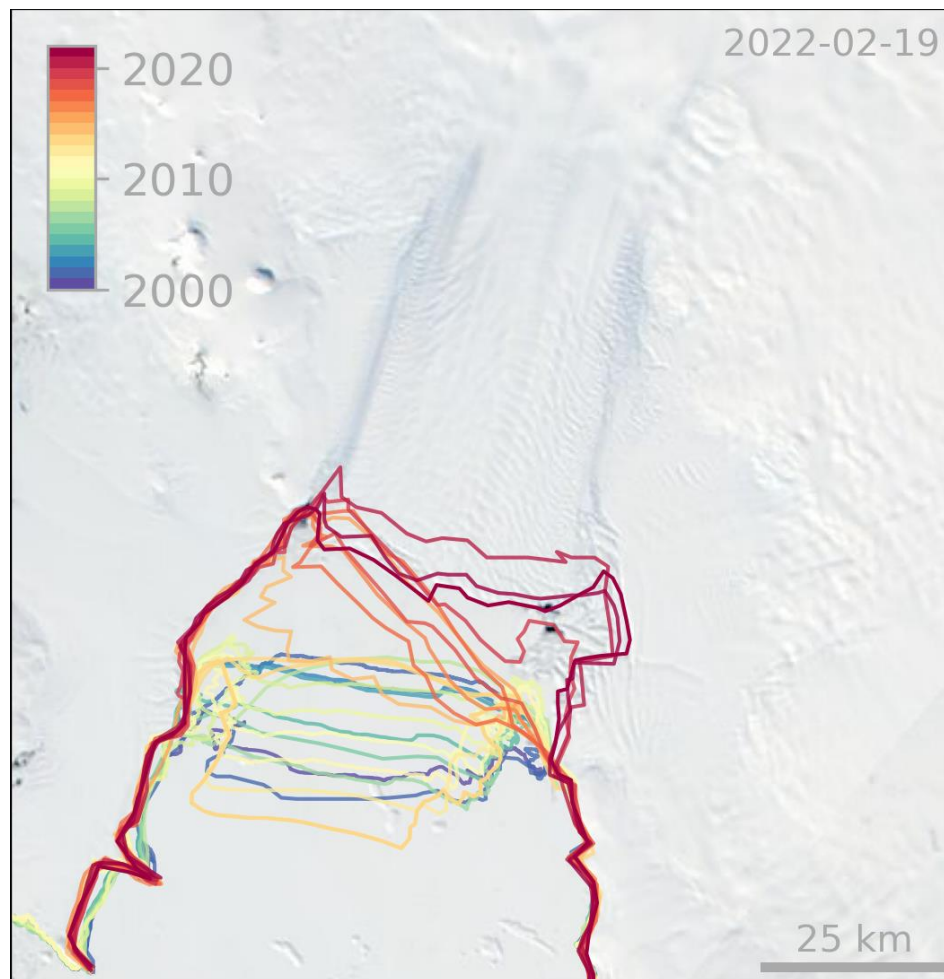


Figure 1: Pine Island Glacier (PIG) and surroundings: (a) Digital elevation map (DEM) at 1 km resolution showing PIG and the Thwaites Glacier (TG). The shading and the black contours show the surface elevation (m), contoured every 500 m and labelled every 1,000 m, while the regions where the ice velocity is equal to 50 m y^{-1} and 200 m y^{-1} are denoted by the thin and thick purple contours, respectively. The ice velocities are estimated using data from the National Snow and Ice Data Center (NSIDC; Rignot et al., 2017). The blue line highlights the ice shelves borders. The red box represents the domain over which the averaging is performed for the time series in Fig. 7 (-101.5°W to -99.5°W and -75.5°S to -74.5°S). (b) 19 February 2022 MODIS satellite image of PIG with an overlay of historical calving fronts since 2000.

57

58 The melting around PIG has been attributed mostly to basal melt and ocean-ice dynamics, in
59 particular to the presence of relatively warm deep water on the Amundsen Sea continental shelf
60 (Jacobs et al., 2011) with the exposure of the grounded ice to the ocean water once the floating ice
61 retreats (Joughin et al., 2021). Calving events themselves can promote further ice loss through the
62 associated ocean mixing that warms up deep water (Meredith et al., 2022). There is, however,
63 considerable interannual variability, in line with changes in ocean currents and local wind stress



64 (Webber et al., 2017). Other factors, such as changes in ice rheology and basal slipperiness (De
65 Rydt et al., 2021), can also explain the recent ice loss at PIG. While ocean dynamics likely account
66 for most of the observed ice loss, atmospheric forcing may also be important in modulating PIG
67 ice loss, as is it has been shown recently to be the case elsewhere in the continent (e.g. Francis et
68 al. 2021, 2022; Greene et al., 2022). Besides atmospheric rivers (Wille et al. 2019, 2021, 2022;
69 Francis et al., 2020) and associated surface radiative warming, one of the meteorological
70 phenomena that can foster ice damage around Antarctica is Foehn winds (Elvidge and Renfrew,
71 2016; Ghiz et al. 2021). The word Foehn, which means “hair dryer” in German, refers to the warm
72 and dry winds that descend on the leeside of a mountain range. During Foehn events, anomalously
73 warm and dry air masses occur in the lee slopes of a mountain range in response to orographic
74 blocking of humid air upwind (Elvidge and Renfrew, 2016). Foehn effects can trigger surface
75 melting and snow or ice sublimation, with melting less likely as the low humidities during Foehn
76 episodes cause large latent heat losses from the snowpack and hence prevent its warming.
77 Additionally, Foehn effects can promote the depletion of the firn air content at the top of the ice
78 shelf with the resulting impermeable ice-surface encouraging meltwater-induced hydrofracture
79 (Bell et al., 2018). Besides, Foehn winds can themselves promote ice breakup through the melting
80 of snow (Bell et al., 2018) and the fostering of calving events (Miles et al., 2017), as an offshore
81 wind direction, combined with ocean swells, aids in the breakup and subsequent drifting of newly
82 formed icebergs (Francis et al., 2022).

83
84 Several studies have reported the occurrence of Foehn around Antarctica such as in the Ross
85 Sea (e.g., Speirs et al., 2013; Zou et al. 2021a, b), PIG (Djournna and Holland, 2021), Vestfold
86 Hills in East Antarctica (Gehring et al., 2022) and Antarctic Peninsula (e.g., Laffin et al., 2021).
87 Zou et al. (2021a, b) investigated the processes behind four major melting events at the Ross Ice
88 Shelf. In three of the four cases Foehn warming occurred for more than 40% of the melting period,
89 and the Foehn effect caused a 2-4°C increase in surface temperature. The authors concluded that
90 Foehn can be an important contributor to surface melting in Antarctica, which can increase the
91 effects of warm and moist air advection. Djournna and Holland (2021) reported Foehn conditions
92 around PIG during March 2013 after the onset of a warm air intrusion associated with an
93 atmospheric river. The combination of warm and moist air advection from lower latitudes and
94 Foehn winds likely explains the record temperature of 17.5°C observed at the northern tip of the
95 Antarctic Peninsula on 24 March 2015 (Bozkurt et al., 2018). A region in Antarctica particularly
96 prone to Foehn effects is the McMurdo Dry Valleys (Speirs et al., 2010): in the presence of a steep
97 pressure gradient, with a ridge over Victoria Land and a low pressure over the Amundsen/Ross
98 Sea, a warming of roughly 30°C in just 3 h has been observed at the valley floor. Speirs et al. (2013)
99 presented a 20-year climatology of Foehn events at McMurdo Dry Valleys from weather station
100 data. They reported positive trends for all seasons during 1999-2008 with a larger magnitude in
101 winter when the large-scale dynamics favour the occurrence of Foehn. The role of Foehn winds in
102 the disintegration and collapse of the Larsen ice shelves A, B and C on the Antarctic Peninsula in
103 1995, 2002 and 2017 respectively, has been widely reported (Cape et al. 2014, 2015; Massom et



104 al., 2018). In fact, during periods of strong westerlies, the warmer and more moist maritime air
105 forced to rise over the mountains in the western Antarctic Peninsula and warms and dries out on
106 the leeside, generating frequent Foehn events over the ice shelves on the eastern side of the
107 peninsula (Laffin et al., 2021). The complex terrain around PIG (Fig. 1a) favours Foehn wind
108 occurrence there as well.

109

110 Laffin et al. (2021), and for the Antarctica Peninsula using a combination of model, surface
111 observations and reanalysis data, found that the Foehn effect accounts for roughly 3% of the total
112 surface melt. However, close to the mountains, this figure can rise to as much as 18%. The number
113 of Foehn days, more so than its strength, explains the annual variability in melting triggered by the
114 Foehn effects. Even though no statistically significant trend in Foehn occurrence is seen in the
115 1979-2018 period, an increased occurrence in the summer and decreased in the other three seasons
116 is detected in 1999-2018. The same study noticed that Foehn days in the austral summer are
117 positively correlated with the Southern Annular Mode (SAM, Marshall et al., 2003), an index
118 which gives an indication of the strength and latitudinal position of the westerlies in the Southern
119 Hemisphere, and negatively correlated with the SAM in the austral autumn. Positive SAM events
120 also foster the occurrence of Foehn in the Antarctic Peninsula owing to the stronger westerly flow
121 (Cape et al., 2015).

122

123 Despite major advances in the understanding of the Antarctic surface mass balance in recent
124 decades, there are still major uncertainties (e.g. The IMBIE team, 2018) in particular in areas that
125 are prone to ice loss such as PIG (Kowalewski et al., 2021). An important process for the surface
126 mass balance is snow evaporation or sublimation (Das et al., 2013; Mottram et al., 2021), which
127 is typically difficult to detect from observations given its nature. Even though Foehn events are
128 believed to play an important role in the surface mass loss around Antarctica (Ghiz et al., 2021),
129 the underlying processes remain unclear. Moreover, no study has examined the occurrence of
130 Foehn on a longer time-scale over PIG even though it is expected to have a significant impact
131 given the steep topography in the region (Fig. 1a). Hence, it is vital to quantify the occurrence of
132 Foehn episodes so as to better understand their role in ice loss through melting and/or sublimation.
133 This is achieved in the present work, where the occurrence of Foehn at PIG and its role in the
134 surface mass balance is investigated using a state-of-the-art reanalysis dataset, satellite imagery
135 and in situ measurements.

136

137 The remainder of the paper is organised as follows. In section 2, the datasets used in this work
138 as well as the Foehn-detection algorithm employed and how the different terms in the surface mass
139 balance are quantified are described. Section 3 provides a discussion of the occurrence and trends
140 of Foehn over PIG, as well as its impacts on the surface mass balance. In Section 4 the focus is on
141 the large-scale conditions that promote the occurrence of Foehn, while a case study in November
142 2011 is discussed in section 5. Section 6 summarises the main findings of the study.

143



144 2. Datasets and Methodology

145 2.1. Observational and Reanalysis Datasets

146 The main dataset used in this study is the ERA-5 reanalysis data (Hersbach et al., 2020),
147 which is available on an hourly basis and on a $0.25^\circ \times 0.25^\circ$ (~27 km) grid from 1950 to present.
148 Both hourly pressure-level (Hersbach et al., 2018a) and surface (Hersbach et al., 2018b) data
149 are considered in this work. ERA-5 is one of the best performing reanalysis datasets around
150 Antarctica in comparison with station observations as noted e.g. by Gossart et al. (2019).

151 The $1 \text{ km} \times 1 \text{ km}$ dataset used for the Digital Elevation Model of Pine Island Glacier (PIG)
152 and surrounding region combines measurements collected by the European Remote Sensing
153 Satellite-1 (ERS-1) Satellite Radar Altimeter from March 1994 to January 1995, and the Ice,
154 Cloud, and land Elevation Satellite (ICESat) Geosciences Laser Altimeter System from
155 February 2003 to March 2008 (Bamber et al., 2009b). The ice velocity for PIG and Thwaites
156 Glacier is estimated from a combination of satellite interferometric and synthetic-aperture radar
157 systems, and is available at a 450 m spatial resolution from 1996 to 2016 (Rignot et al., 2016).
158 Sentinel 2 satellite data, downloaded from Copernicus website (Copernicus, 2022), is used to
159 extract the sea-ice front at PIG.

160 Surface radiation fluxes from the Clouds and Earth's Radiant Energy System (CERES;
161 Doelling et al. 2013, 2016) dataset are available on an hourly basis at $1^\circ \times 1^\circ$ resolution from
162 March 2000 to present. The CERES product used here is the SYN1deg - Level 3, which is freely
163 available online (NASA/LARC/SD/ASDC, 2017).

164
165 10-min air temperature observations at the Evans Knoll station (-74.85°S , -100.404°W ; 188
166 m above sea-level) located just to the northeast of PIG are freely available at the Antarctic
167 Meteorological Research Center & Automatic Weather Stations Project website, Space Science
168 and Engineering Center, University of Wisconsin-Madison (Lazzara et al., 2022).

169
170 The surface melt area is estimated using measurements collected by the Moderate Resolution
171 Imaging Spectroradiometer (MODIS; Kaufman et al., 1997) on board the National Aeronautic
172 and Space Administration's Terra and Aqua satellites. In particular, the daily global surface
173 reflectance Level 3 data at $0.05^\circ \times 0.05^\circ$ spatial resolution (MODIS products MOD09CMG and
174 MYD09CMG for Terra and Aqua, respectively; Vermote 2015a,b) is downloaded, and the
175 enhanced Normalised Difference Water Index (NDWI) defined in Moussavi et al. (2016) is
176 estimated. The NDWI index makes use of the reflectance contrast between water and ice in the
177 red (630-690 nm) and blue (450-510 nm) bands.



178 2.2. Foehn-Detection Algorithm

179 Foehn events at PIG are identified using a modified version of the algorithm proposed by
180 Laffin et al. (2021), in which the authors studied Foehn episodes in the Antarctic Peninsula
181 using ERA-5, model and observational data. A given hourly time-step is denoted as a Foehn
182 time-step if the following three conditions hold:

$$183 \left\{ \begin{array}{l} 2m \text{ Temperature} > 60^{th} \text{ Percentile} \\ 2m \text{ Relative Humidity} < 30^{th} \text{ Percentile} \\ 10m \text{ Wind Speed} > 60^{th} \text{ Percentile} \end{array} \right. \quad (1)$$

185 where the temperature, relative humidity (RH) and wind speed are extracted from ERA-5,
186 and the algorithm is applied in a $10^\circ \times 10^\circ$ domain ($105^\circ\text{-}95^\circ\text{W}$, $80^\circ\text{-}70^\circ\text{S}$) centered on PIG. The
187 thresholds are grid-point dependent, and while the RH and wind speed thresholds are computed
188 over the full 40-year period (1980-2020), hourly thresholds for each month are used for the air
189 temperature to account for the annual cycle. Laffin et al. (2021) used a threshold of 0°C for the
190 temperature as the focus was on Foehn events that cause surface melt. However, such a
191 threshold is hardly met at PIG (Moncada and Holland, 2019; Djoumna and Holland, 2021) given
192 its poleward location compared to the Antarctic Peninsula ($\sim 75^\circ\text{S}$ vs. $\sim 60^\circ\text{-}70^\circ\text{S}$) and resulting
193 reduced exposure to the warmer lower-latitude air. It is important to note, however, that a
194 surface or air temperature above 0°C is not needed for surface melting to take place. As noted
195 by Ghiz et al. (2021), melting can occur at surface and air temperatures below freezing provided
196 the melt energy, given by the sum of the surface radiation, turbulent and ground heat fluxes, is
197 positive for at least two diurnal cycles. In addition to melting, Foehn promotes snow sublimation
198 (Kirchgaessner et al., 2021) and depletes firn air content from ice shelves, which encourages
199 meltwater-induced hydrofracture (Bell et al., 2018). Given this, the 60th percentile of the air
200 temperature is used as the temperature threshold instead, in line with that considered for the
201 wind speed but taking into account the strong annual variability in the region. The threshold
202 values range from about 2 to 12 m s^{-1} for the 10-m wind speed, 232 K to 274 K for the 2-m air
203 temperature, and 59 to 82% for the 2-m relative humidity.

205
206 It is important to note that ERA-5 reanalysis data lacks the spatial resolution to properly
207 resolve smaller-scale flows, and therefore may not give a full picture of Foehn around PIG.
208 However, the findings of Laffin et al. (2021) suggest that its representation of Foehn, at least in
209 the Antarctic Peninsula, is accurate enough in particular for moderate and strong episodes to
210 justify its use here. In particular, these authors found that the reanalysis captured roughly 92%
211 of the Foehn events detected with in situ weather station data. The biases in the ERA-5 radiative
212 fluxes, which in a comparison with in situ observations at Siple Dome next to the Ross Ice Shelf
213 are as large as 100 W m^{-2} for the downward shortwave and 50 W m^{-2} for the downward longwave
214 (Ghiz et al., 2021), suggest that a Foehn identification algorithm based on the surface energy
215 budget, and using ERA-5 data, may not be optimal for Antarctica.



216 2.3. Surface Mass Balance

217 Over snowy regions such as Antarctica, and following Dery and Yau (1999, 2002) and
 218 Scarchilli et al. (2010), the surface mass balance can be expressed as

219

$$220 \quad S = P - E - M - Q_{snow} - D \quad (2)$$

221

222 where S is the rate of accumulation or storage of snow at the surface, P is the precipitation
 223 (snowfall) rate, E is the surface evaporation rate which includes the sublimation rate (Q_{surf}),
 224 M represents the surface melt and runoff rate, Q_{snow} is the blowing snow sublimation rate and
 225 D is the blowing snow divergence rate. All terms are expressed as mm of water equivalent per
 226 day (mm w.e. day⁻¹).

227

228 In ERA-5, snow is regarded as an additional layer on top of the soil layer, and is characterized
 229 by a snow temperature T_{sn} , with independent and prognostic thermal and mass contents. Snow
 230 melting takes place if T_{sn} exceeds the melting point (273.16 K), while snow sublimation is
 231 estimated with the bulk aerodynamic formula using the wind speed and specific humidity of the
 232 lowest model layer and the saturated specific humidity at T_{sn} (ECMWF, 2016). The bulk
 233 aerodynamic formula, used in ERA-5, performed well in estimating the observed snow
 234 sublimation over the Himalayas (Stitger et al., 2018), but has not been evaluated over
 235 Antarctica. What is more, blowing snow is not accounted for in the reanalysis dataset, which is
 236 problematic as during Foehn events it is known to lower the albedo and increase surface
 237 compaction, and hence enhance the effects of Foehn on the snowpack (e.g. Bromwich, 1989;
 238 Scarchilli et al., 2010; MacDonald et al., 2018; Datta et al., 2019; Pradhananga and Pomeroy,
 239 2022). As a result, the terms Q_{surf} , D and Q_{snow} in Eq. (2) are estimated as detailed below,
 240 while P and M are taken directly from the reanalysis. All constants are defined in Table 1.

241

242 The surface sublimation rate, Q_{surf} , included in the term E in Eq. (2), is parameterized as

$$243 \quad Q_{surf} = \rho' \frac{\rho_{air} \overline{(w'q')}}{\rho_{water}} = \rho' \frac{\rho_{air} (u_* q_*)}{\rho_{water}} \quad (3)$$

244 with

245

$$u_* = \frac{\kappa U}{\ln\left(\frac{z + z_0}{z_0}\right)}$$

246

247

$$q_* = \frac{\kappa q_{si} (RH_{ice} - 1)}{\ln\left(\frac{z + z_q}{z_q}\right)}$$



248 where u_* is the friction velocity, q_* is a humidity scale, κ is the von Karman constant, U is the
 249 wind speed at height z above the surface (taken to be 10-m), z_0 is the aerodynamic roughness
 250 length, q_{si} is the saturation mixing ratio over ice, RH_{ice} is the relative humidity with respect to
 251 ice, z_q is the roughness length for moisture over snow (taken to be the same as z_0), ρ is the air
 252 density, ρ_{water} is the density of water, and ρ' is a conversion factor from m s^{-1} to mm day^{-1} . If
 253 $RH_{ice} > 1$, q_* becomes positive and deposition to the surface is said to occur. The term $\overline{(w'q')}$
 254 is the turbulent moisture flux at the surface, with $\rho_{air}\overline{(w'q')}$ giving the sublimation rate (van
 255 den Broeke, 1997). The rate of water equivalent lost to sublimation is obtained by dividing the
 256 sublimation rate by the density of water, as done by Montesi et al. (2004).

257
 258 The blowing snow sublimation rate, Q_{snow} , is expressed as in Eq. (4) below

259
 260
$$Q_{snow} = \frac{a_0 + a_1\xi + a_2\xi^2 + a_3\xi^3 + a_4U_{10} + a_5\xi U_{10} + a_6\xi^2 U_{10} + a_7U_{10}^2 + a_8\xi U_{10}^2 + a_9U_{10}^3}{U'} \quad (4)$$

261 with

262
 263
$$\xi = \frac{RH_{ice} - 1}{2\rho_{ice}[F_k(T) + F_d(T)]}$$

264
 265
$$U' = \frac{(1 - U_t/U_{10})^{2.59}}{(1 - 6.975/U_{10})^{2.59}}$$

266
 267
$$U_t = 6.975 + 0.0033 (T_{2m} + 27.27)^2$$

268
 269 where ξ is a thermodynamic term, U_{10} is the 10-m wind speed, U' is a non-dimensional factor that
 270 removes the dependence on the saltation mixing ratio, U_t is the threshold for initiation of blowing
 271 snow, T_{2m} is the 2-m temperature, ρ_{ice} is the density of ice, and $F_k(T)$ and $F_d(T)$ are the
 272 conductivity and diffusion terms associated with sublimation, both temperature dependent and
 273 extracted from Rogers and Yau (1989). While negative values of Q_{surf} indicate sublimation and
 274 positive values denote deposition, the opposite is true for Q_{snow} , with positive values implying
 275 sublimation of blowing snow is taking place.

276
 277 The snow transport rate, Q_t , is a vector quantity whose magnitude is given by

278
$$Q_t = BU_{10}^c \quad (5)$$

279 with the direction obtained by projecting it onto the 10-m horizontal wind vector. The divergence
 280 term D in Eq. (2) is then obtained by

281
$$D = \frac{\rho'}{\rho_{water}} \nabla \cdot \mathbf{Q}_t \quad (6)$$



Constant	Value	Constant	Value
a_0	3.78407×10^{-1}	a_8	1.56862×10^{-3}
a_1	-8.64089×10^{-2}	a_9	-2.93002×10^{-4}
a_2	-1.60570×10^{-2}	κ	0.4
a_3	7.25516×10^{-4}	ρ'	8.6400×10^7
a_4	-1.25650×10^{-1}	ρ_{water}	1000 kg m^{-3}
a_5	2.48430×10^{-2}	ρ_{ice}	917 kg m^{-3}
a_6	-9.56871×10^{-4}	B	$2.2 \times 10^{-6} \text{ kg m}^{-5.04} \text{ s}^{3.04}$
a_7	1.24600×10^{-2}	C	4.04

Table 1: Constants used in the surface mass balance.

282
 283
 284

285 3. Foehn Events at PIG and Impacts on Ice

286 The statistics of Foehn events at PIG are summarized in Fig. 2. Foehn is more frequent in the
 287 austral winter season, in particular from June to October, and less common in the summer albeit
 288 with a considerable spread in all months (Fig. 2a). The annual cycle in the duration of Foehn events
 289 is less pronounced, with monthly-mean values in the range 5 to 9 h, with August featuring both the
 290 highest number (~123) and longest (~9 h) Foehn episodes. At the Antarctic Peninsula, Foehn
 291 occurrence peaks in the transition seasons (Wiesenekker et al., 2018; Laffin et al., 2021) whereas
 292 at the McMurdo Dry Valleys located next to the Ross Sea it is more frequent in winter (Speirs et
 293 al., 2013). As Foehn events are driven by large-scale pressure gradients, the difference in the
 294 timing of the peaks is likely a result of the variability in the position of the baroclinic systems. In
 295 particular, and as noted by Simmonds et al. (2003), the cyclonic activity in the Ross Sea, northern
 296 Antarctic Peninsula and around PIG is maximized in winter whereas in the central Antarctic
 297 Peninsula it is the highest in the summer. Consistent with this, in the Amundsen and
 298 Bellingshausen Seas there is a pronounced equatorward shift in the mid-latitude storm track in the
 299 summer months (Dias da Silva et al., 2021), which is in line with the higher occurrence of Foehn
 300 at PIG in the colder months. The Amundsen Sea Low (ASL), a semi-permanent low pressure in
 301 the Amundsen-Bellingshausen Seas (60°-75°S and 170°-290°E) that exhibits the largest
 302 geopotential height variability in the Southern Hemisphere, is likely to play a major role in the
 303 occurrence of Foehn at PIG (McLennan and Lenaerts, 2021). Meridionally, it is at its most poleward
 304 location in late winter and is shifted further equatorwards in the summer, while longitudinally it is
 305 the closest to PIG in the summer months (Raphael et al., 2016). As Foehn is more likely when the



306 ASL is just to north of PIG with its clockwise circulation encouraging Foehn effects in the region,
307 as noted in section 4, the intricate annual cycle of the ASL may explain the highest Foehn
308 occurrence in late winter and why it still takes place in the summer months. In the area around
309 PIG, there are on average 3.0 Foehn days in the month of August (123 occurrences over the 41-
310 year period 1980-2020) lasting roughly 7.9 h each, whereas in January there are 0.37 Foehn days
311 per month that typically last for about 5.1 h. Wiesenekker et al. (2018) reported an average of 1.3
312 to 5.8 Foehn events per month in the Antarctic Peninsula over 1979-2016, with roughly 70-80%
313 of the events in December 2014 - December 2016 lasting less than a day. These figures are higher
314 than those at PIG shown in Fig. 2a, which is due to the fact that the Antarctic Peninsula is more
315 exposed to the mid-latitude storm track, with the higher terrain on its western side promoting Foehn
316 effects.

317

318 Fig. 2b gives the area-averaged air temperature and sensible heat flux for the Foehn events, with
319 the air temperature, sensible heat flux and RH anomalies during Foehn episodes plotted in Fig. 2c.
320 The sensible heat flux is positive, and hence directed downwards towards the surface, with
321 monthly-mean values in the range 18 to 42 W m⁻², with higher values in the winter months. This is
322 in line with Laffin et al. (2021) and with the fact that the sensible heat flux around Antarctica is
323 maximized in the colder months when the surface to air temperature gradient is the highest, owing
324 to the sharp thermal inversions that develop at this time of the year (Reijmer et al., 1999). The
325 magnitude of the fluxes is comparable to that modeled over the Antarctica Peninsula (e.g. Elvidge
326 et al., 2014) and at Joyce Glacier in McMurdo Dry Valleys (Hofsteenge et al., 2022). The air
327 temperature during Foehn events at PIG is below freezing, ranging from -7°C in January to -22°C
328 in August. However, melting and sublimation can still occur, in particular when accounting for the
329 large variability which is maximized in the summer (e.g., Ghiz et al. 2021). Fig. 2c shows that
330 Foehn effects lead to generally warmer (air temperatures anomalies typically of +0-7°C) and drier
331 (RH anomalies in the range -8% to -11%) weather conditions accompanied with a downward
332 sensible heat flux (anomalies of +14-21 W m⁻²).

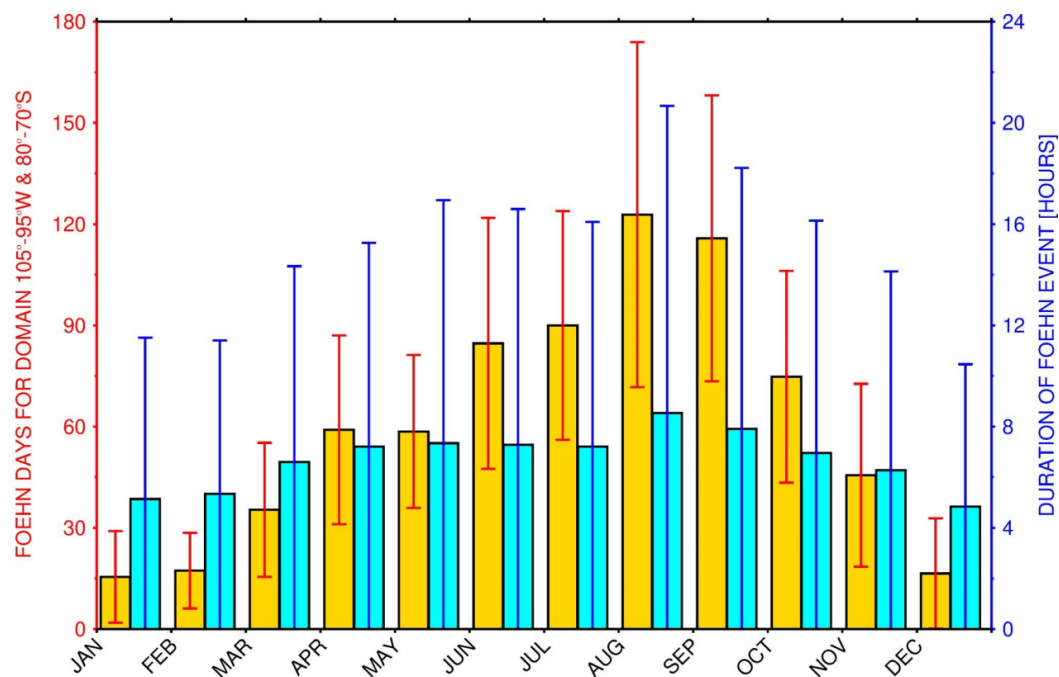
333

334 Fig. 2d gives the trends in the number of Foehn days and in the duration of Foehn events for
335 1980-2020. A positive trend is present in the former even though the slope, of ~0.1 days year⁻¹, is
336 not statistically significant at the 95% confidence level, while the trend in the duration of Foehn
337 events is negligible. An inspection of the trends for individual seasons revealed that only the one
338 in the duration of Foehn events for the autumn season is statistically significant, with a slope of
339 about -0.002 days year⁻¹ (not shown). Studies of trends of Foehn occurrence in Antarctica also
340 reported non statistically significant slopes, in particular over the two major studied regions of the
341 McMurdo Dry Valleys (e.g., Speirs et al., 2013) and the Antarctic Peninsula (e.g., Laffin et al.,
342 2021). However, Cape et al. (2015), and for a single long-term station to the north of the Larsen C
343 Ice Shelf east of the Antarctic Peninsula, found a positive trend in the summer months of about
344 1.46% year⁻¹ for the period 1962-2010 statistically significant at the 95% confidence level. Fig. 2d
345 also shows considerable inter-annual variability in both the number and duration of Foehn days.

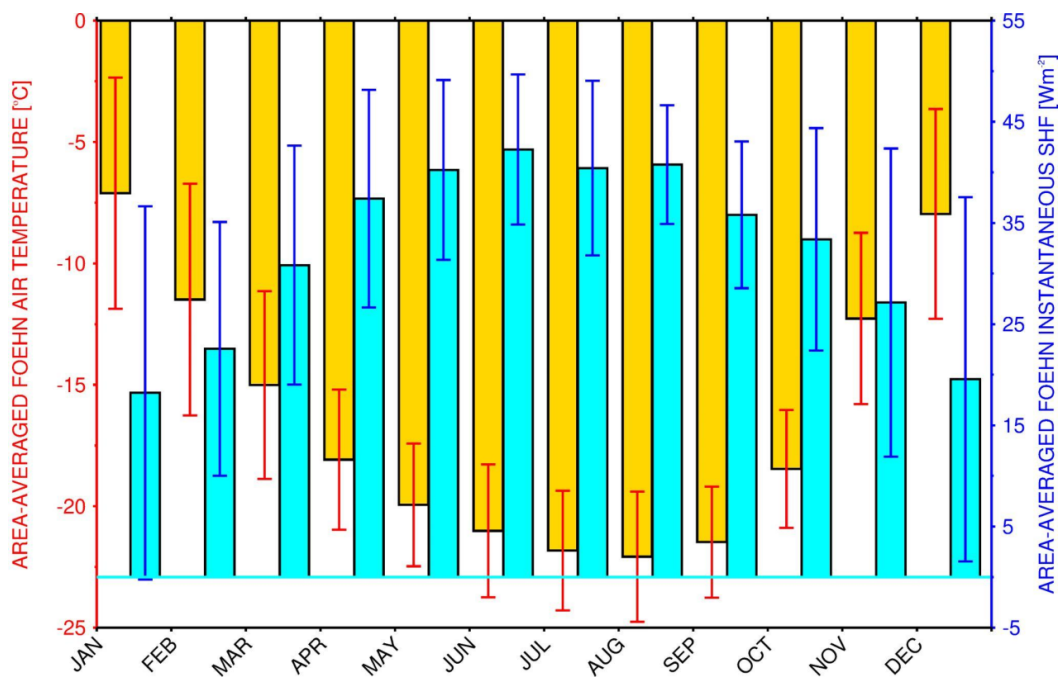


346 The major peaks taking place mostly in La Nina (1984, 1985, 1999, 2010) or neutral (1981, 1993,
347 1996, 1999, 2003, 2008, 2013) years, while the minimum in 1982, 1986, 1997 and 2015 coincide
348 with El Nino years (Lestari and Koh, 2016; Zhang et al., 2022). In La Nina conditions, the ASL is
349 more active than normal (Raphael et al., 2016), which may promote the occurrence of Foehn, while
350 in El Nino episodes the presence of a ridge over the Amundsen and Bellingshausen Seas (Yuan,
351 2004) may discourage Foehn effects at PIG. A discussion of the large-scale patterns that favor
352 Foehn occurrence at PIG is given in section 4.
353
354

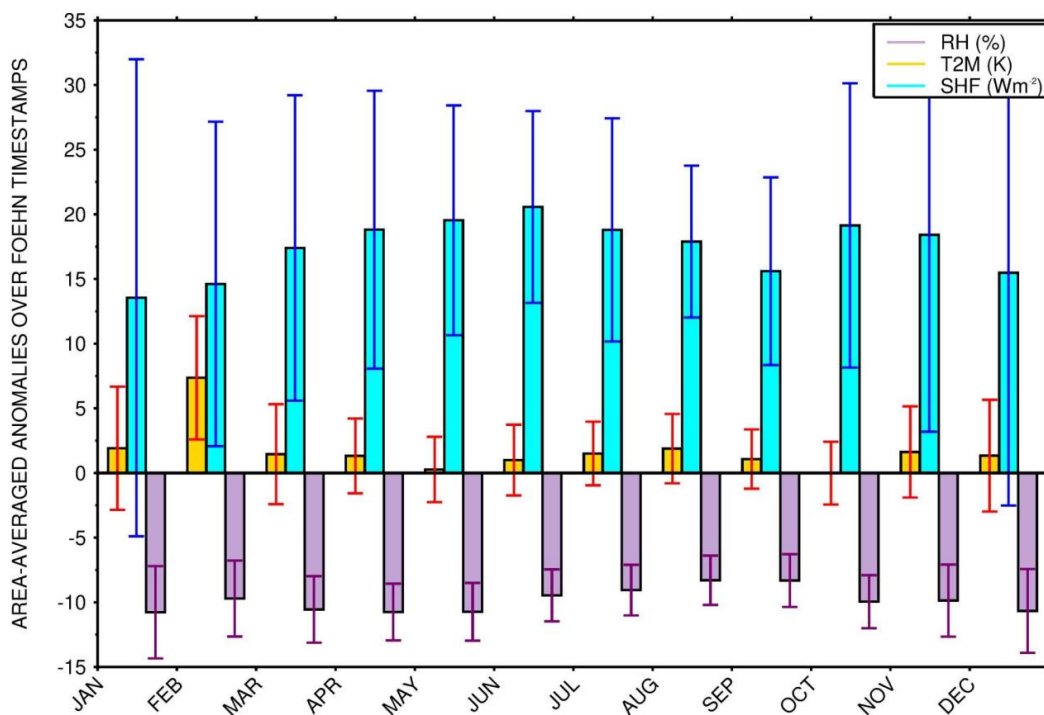
(a)



(b)



(c)



(d)

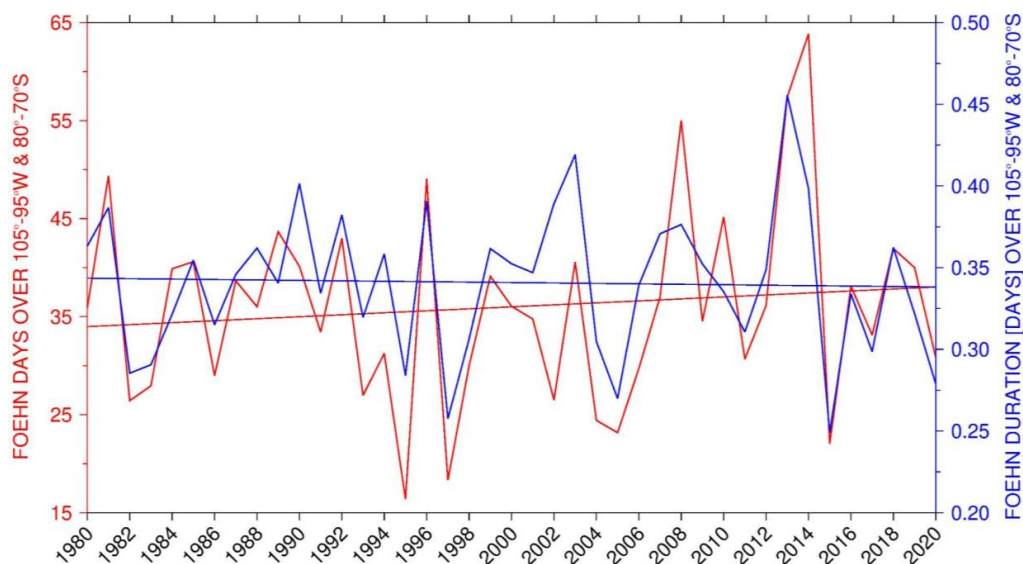


Figure 2: Climatology and trends of Foehn events: (a) Monthly mean (histogram bars) and standard deviation (error bars) of Foehn days (orange; left axis) and duration of Foehn events (hours; blue; right axis) for the period



1980-2020 and for the domain 95°W-105°W and 80°S-70°S. (b) is as (a) but for the area-averaged air temperature (°C; orange; left axis) and instantaneous sensible heat flux (W m^{-2} ; blue; right axis; positive if downwards towards the surface). (c) gives the air temperature (°C; orange), instantaneous sensible heat flux (W m^{-2} ; blue) and relative humidity (%; purple) anomalies during Foehn timestamps. (d) Trend in Foehn days (left; red) and in the duration of Foehn events (right; blue) for 1980-2020. The slopes of the Foehn days and duration are $0.101024 \text{ days yr}^{-1}$ and $-0.0001 \text{ days yr}^{-1}$ with a statistical significance of 55% and 18%, respectively.

355 A quantification of the potential for surface melting and sublimation is presented in Fig. 3. The
356 “melt potential” index (MPI) is defined following Orr et al. (2022) using the daily maximum air
357 temperature for 1980-2020, for both the full year and extended summer season (November to
358 February, NDJF). At each grid-point, the MPI intensity is given by the difference between the 95th
359 percentile of the daily maximum air temperature distribution and the melt threshold of 273.15 K,
360 while the MPI frequency is the percentage of values higher than the threshold. The “sublimation
361 potential” index (SPI) is defined in the same way but using the 95th percentile of the daily
362 maximum of the hourly surface sublimation given by Eq. (3) and a threshold of zero, while its
363 frequency expresses the percentage of the days in the 1980-2020 period when there is sublimation
364 for at least one hour per day at the site.

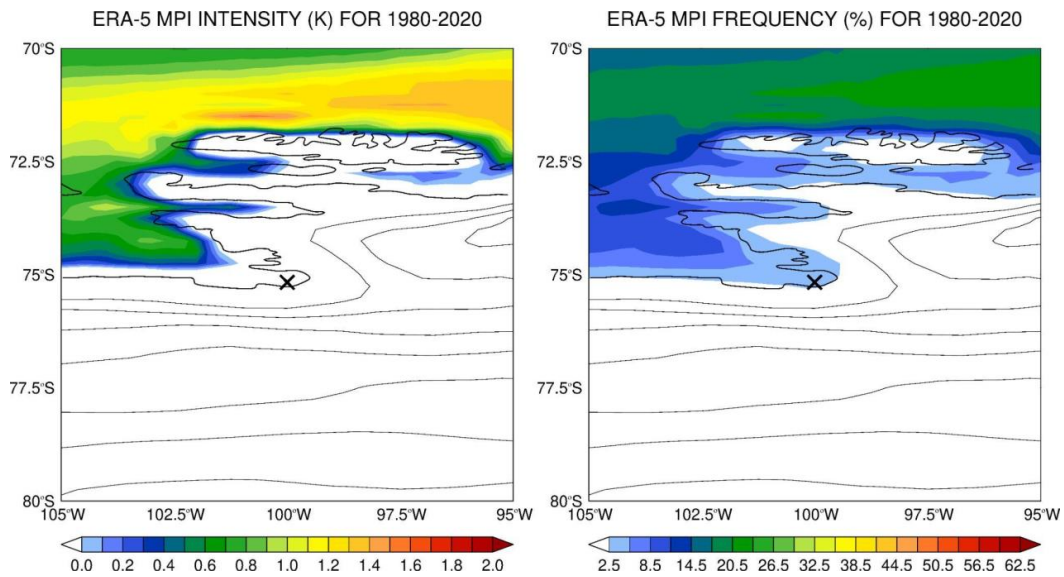
365

366 Surface melting is not common at PIG and is mostly restricted to the warmer months, with a MPI
367 intensity of 0.87 K and a frequency of around 10% in NDJF 1980-2020, whereas when taking the
368 full year both values are -0.27 K and ~4%, respectively. Orr et al. (2022), and using higher spatial
369 resolution (~12 km) modelling products over December-February 1979-2019, obtained values of
370 1.3-1.7 K and 23.7-23.8%. Surface sublimation at PIG is also more likely in the summer months,
371 albeit the differences between the full year and NDJF are small, with magnitudes of about 3.34
372 and 3.39 mm w.e. day⁻¹, respectively, and a frequency of occurrence around 100%. The fact that
373 the frequency is very high indicates that the daily maximum in the surface sublimation is positive
374 nearly all the time at PIG, suggesting that it is a regular occurrence at the site. Surface melting is
375 confined to lower elevations where the temperature is higher. Here, there is also increasing
376 exposure to the warmer and more moist maritime air masses compared to the high terrain inland.
377 Surface sublimation increases with the wind speed and air temperature, in line with the way it is
378 parameterized, Eq. (3). Even though the near-surface wind is stronger in the colder months (cf.
379 Figs. 3c-d), the higher air temperatures in the summer decrease the supersaturation with respect to
380 ice and hence promote the occurrence of sublimation. Windier and drier conditions, seen in Foehn
381 events (Fig. 2c), also encourage surface sublimation. The convergence of the near-surface wind in
382 the PIG basin and the lower heights and consequently higher temperatures explain the maximum
383 in surface sublimation in the region seen in Figs. 3c-d.

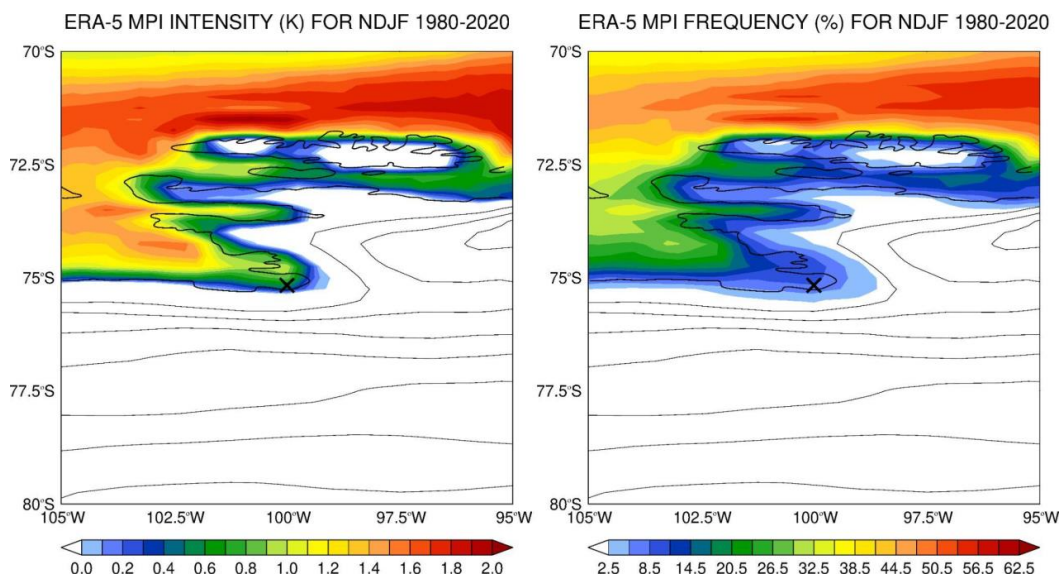
384

385

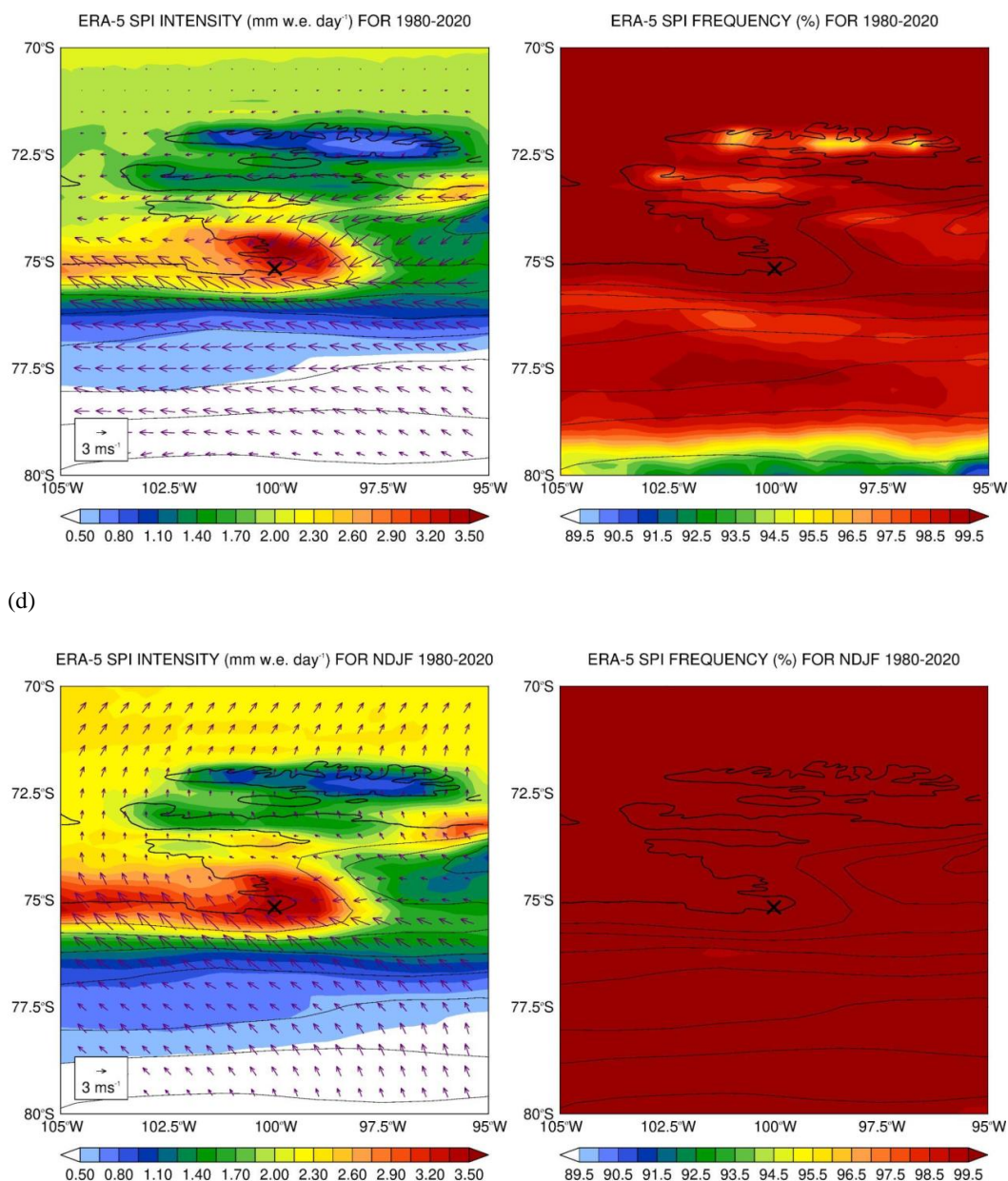
(a)



(b)



(c)



(d)

Figure 3: Melt and Sublimation Potential Indices: (a) “Melt Potential” index (MPI) intensity (K; left) and frequency (%; right), defined following Orr et al. (2022), for 1980-2020. The thin black lines are 250 m orography contours and the land-sea mask is represented by the thick black line. The cross gives PIG location (100°W, 75°10’S). (b) is as (a) but for November-February (NDJF) only. (c)-(d) are as (a)-(b) but for the “Sublimation Potential” index (SPI), with the intensity given in mm of water equivalent per day (mm w.e. day⁻¹). The averaged 10-m horizontal wind vectors are drawn as arrows in the left panels of (c)-(d) for the respective period.



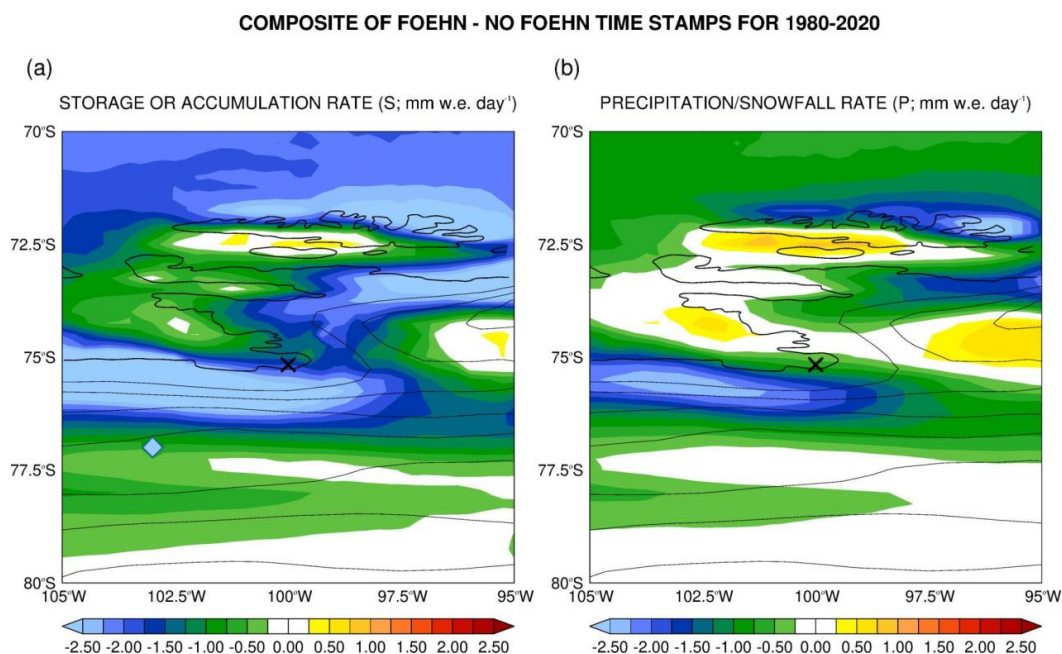
In order to explore the contribution of Foehn to the surface mass balance, Figs. 4a-f show the composite difference of the terms in Eq. (2) between Foehn and no-Foehn timestamps for 1980-2020. The values of S , P , M , Q_{surf} , Q_{snow} and D at PIG are -1.411, -0.345, -0.005, -1.434, 0 and -0.363 mm w.e. day⁻¹, respectively. This indicates that (i) surface sublimation plays the dominant role in the surface mass balance during Foehn events (note that negative values of Q_{surf} and positive values of Q_{snow} indicate sublimation); (ii) the sum of the two blowing snow terms has a magnitude comparable to that of the precipitation/snowfall, roughly 25% smaller than that of the surface evaporation, but with the opposite sign in Eq. (2) reflecting a lack of snowfall during Foehn episodes due to the drier conditions while the convergence of blowing snow at the glacier basin adds to the surface mass; (iii) snow melting makes a negligible contribution to the surface mass balance, being roughly three orders of magnitude smaller than the surface sublimation.

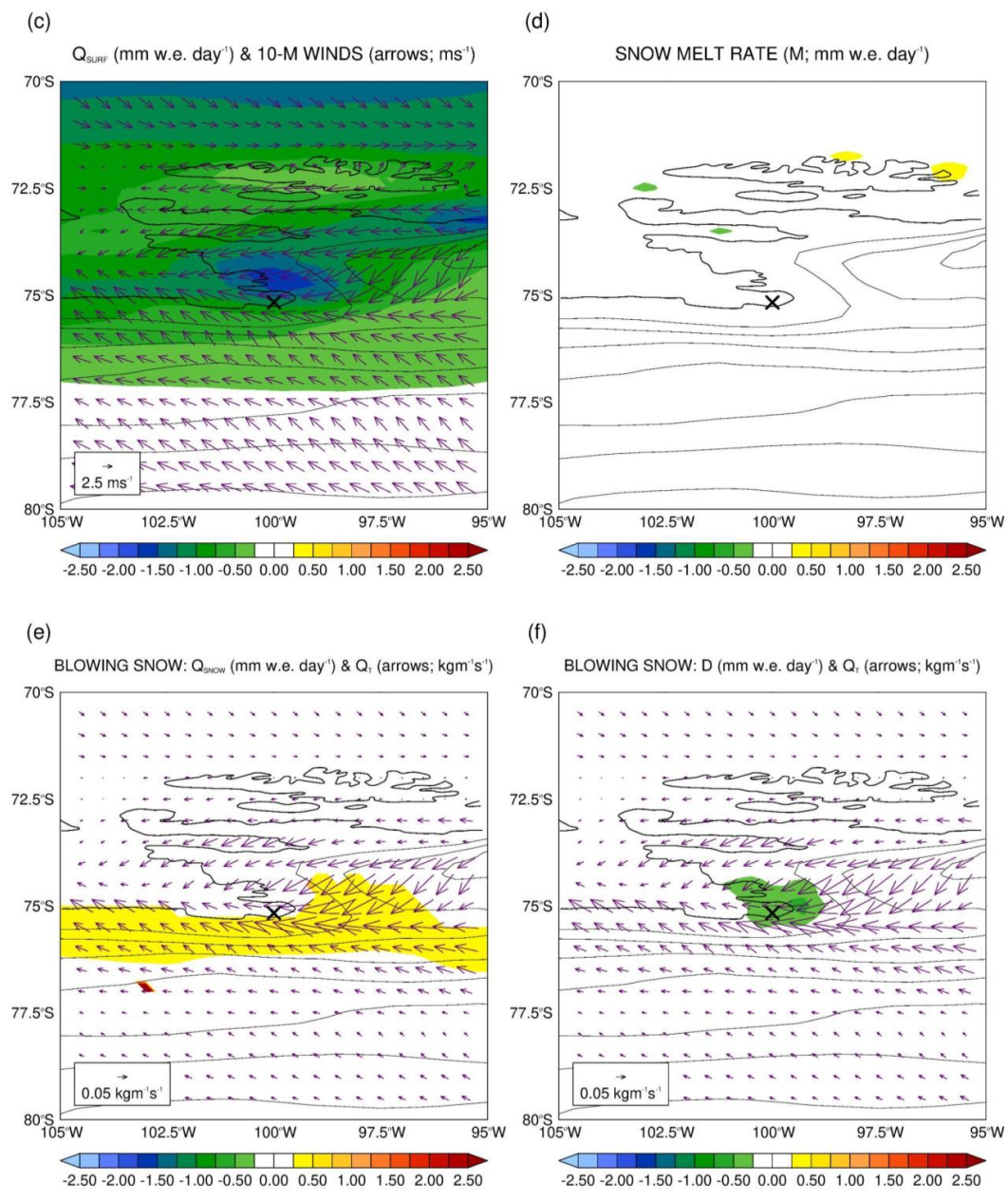
The surface sublimation rate (Fig. 4c) is considerable, with the values at PIG comparable to the maximum rates at a site in northern Victoria Land during November 2018 (Ponti et al., 2021), four times larger than that estimated just off East Antarctica in late winter 2007 (Toyota et al., 2011), but smaller than those at individual events at the Princess Elizabeth base in East Antarctica (Gorodetskaya et al., 2015). The magnitude of the surface sublimation rate during Foehn events is roughly an order of magnitude smaller than that due to melting resulting from ice dynamics at the Ronne Ice Shelf in the Weddell Sea (Holland et al., 2007), Totten Ice Shelf in East Antarctica (Rintoul et al., 2016), and at PIG and Thwaites Glacier in West Antarctica (Feldmann et al., 2019). Yang et al. (2010) compared the surface sublimation given by Eq. (3) with that estimated from a mesoscale model over the Arctic. They found that, for the boreal winter of 2006/2007, the spatial pattern was similar but the magnitude of the sublimation given by the model was larger than that estimated from the empirical formula. The coarse resolution of the ERA-5 data may lead to an underprediction of the strength of the near-surface wind and hence an underestimation of the surface sublimation. As noted before, the surface sublimation increases with the air temperature and wind speed, with both larger at PIG which explains the local maximum at the glacier basin. Surface melting is negligible and confined to the coastal regions further north (Fig. 4d). As noted by Scarchilli et al. (2010), and in line with our findings (Figs. 4e-f), blowing snow plays an important role in the surface mass balance during strong wind (here Foehn) episodes. The magnitude of the total blowing snow sublimation and transport reported in that study, which are measured at the Terra Nova Bay in the Ross Sea, are larger than those estimated here at PIG. This is consistent with the fact that katabatic wind events at Terra Nova Bay can be quite strong, being associated with much higher wind speeds than those during the Foehn events discussed here (Aulicino et al., 2018). Blowing snow sublimation (Fig. 4e) peaks just south and east of the glacier, with values in the range 0.5-0.75 mm w.e. day⁻¹, where the wind speed exceeds the threshold for blowing snow sublimation, Eq. (4). The convergence of the blowing snow transport rate from the east and southeast of PIG leads to the negative



divergence at the basin (Fig. 4f). The negative values in the snowfall rate plot to the south and north of FIG, Fig. 4b, reflect the reduced precipitation in association with the Foehn events. The changes in the storage term between Foehn and no-Foehn timestamps, Fig. 4a, are comparable to the modelled surface mass balance in the region (Donat-Magnin et al., 2021), suggesting that Foehn events are a major contributor to it. Figs. 4g-h gives the differences in the 10-m wind speed and sensible heat flux. During Foehn episodes, there is a strengthening of the near-surface wind by 5-10 ms^{-1} with it converging into FIG. The sensible heat flux increases by about 30-40 W m^{-2} , in line with the area-averaged values in Fig. 2b. While in other regions of Antarctica, such as the Antarctica Peninsula, Foehn plays an active role in snow melting (Laffin et al., 2021), at FIG it seems to trigger mostly sublimation.

386





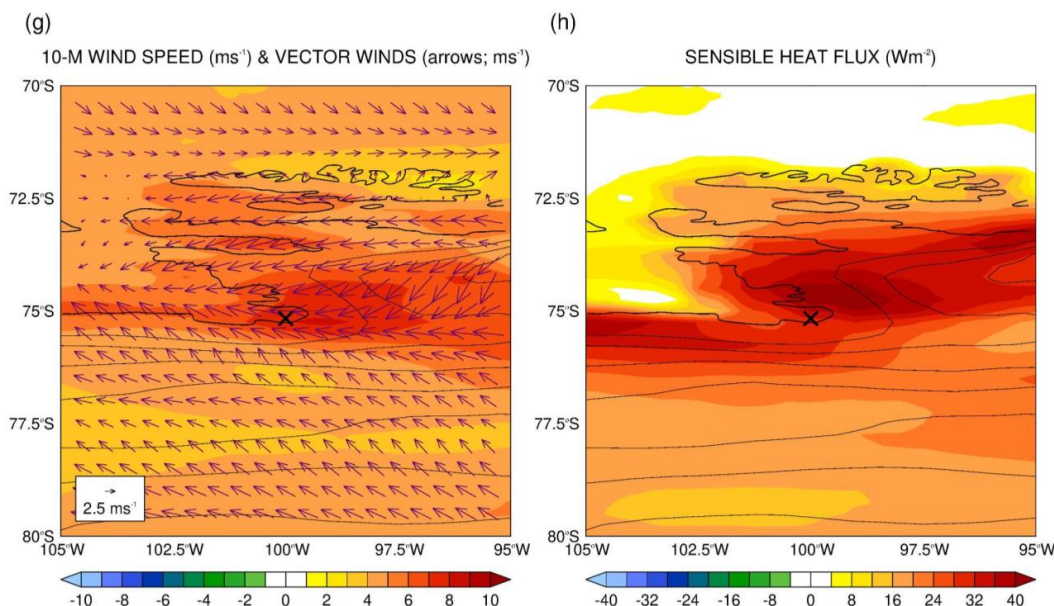


Figure 4: Composite difference between Foehn and no-Foehn timestamps for 1980-2020: (a) Storage or accumulation rate of snow at the surface (S in Eq. (2); mm w.e. day⁻¹), (b) precipitation/snowfall rate (P ; mm w.e. day⁻¹), (c) surface sublimation rate (Q_{surf} ; mm w.e. day⁻¹; positive values indicate deposition to the surface and negative values indicate sublimation), (d) snow melt rate (M ; mm w.e. day⁻¹; positive values indicate melting), blowing snow (e) sublimation rate (Q_{snow} ; mm w.e. day⁻¹; positive values indicate sublimation) and (f) divergence rate (D ; mm w.e. day⁻¹), (g) 10-m wind speed (shading; ms⁻¹) and (h) instantaneous surface sensible heat flux ($W m^{-2}$, positive if downwards towards the surface). The arrows in (c) and (g) give the 10-m horizontal wind vectors (m s⁻¹) while in (e)-(f) they show the blowing snow transport rate (Q_t ; kg m⁻¹ s⁻¹).

387 4. Large-scale Circulation Favorable for Foehn Occurrence

388 Foehn events are driven by large-scale pressure gradients, so it is of interest to investigate the
 389 patterns in the atmospheric circulation which promote their occurrence around PIG. The k-means
 390 clustering technique (Steinley, 2006) is applied to the daily 200 hPa and 850 hPa geopotential
 391 height and wind anomalies and to the sea-level pressure and 10-m wind anomalies for the Foehn
 392 days identified in 2000-2020. However, and to exclude localized events, only days when Foehn
 393 occurred in at least 10% of the 105°-95°W and 70°-80°S region are considered, leaving 1181 days
 394 for the analysis. A different number of clusters from one to five are tested, and the optimal number,
 395 as determined by a silhouette analysis (Rousseeux, 1987), is found to be two (not shown). Cluster
 396 1 (Antarctic Oscillation, AAO; Figs. 5a-b) accounts for ~58% of the total Foehn events and cluster
 397 2 (SAM; Figs. 5c-d) accounts for ~42% of the 1181 Foehn episodes. The clusters' annual cycle is
 398 given in Fig. 5e.
 399



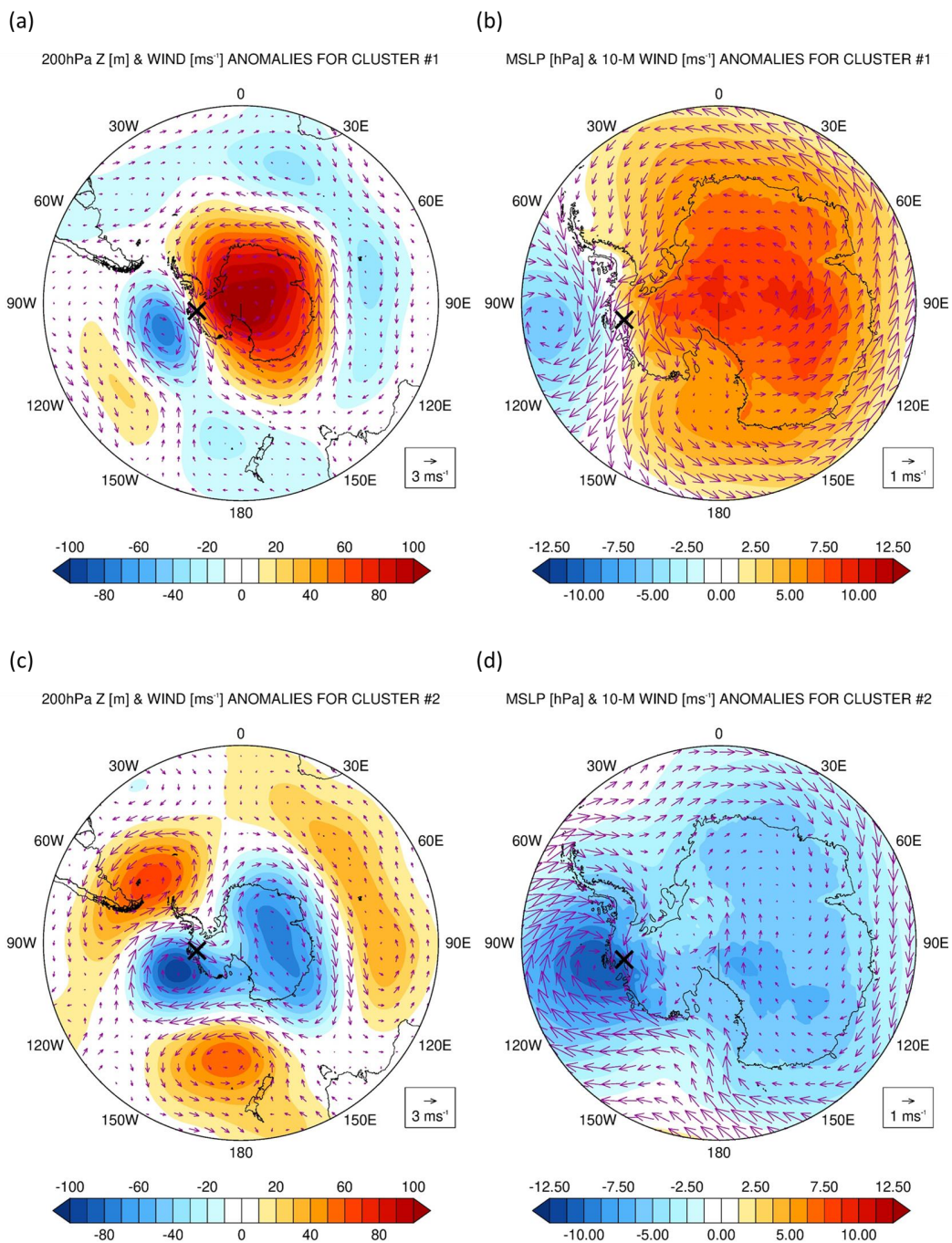
400 The first cluster (Fig. 5a) comprises a wavenumber #1 with an equatorward shift in the mid-
401 latitude storm track as evidenced by the high pressure over Antarctica and a nearly circumglobal
402 low pressure equatorwards. It corresponds to the negative phase of the AAO (Gong and Wang,
403 1999), with the easterly to northeasterly winds around PIG promoting the occurrence of Foehn.
404 The air mass comes from the Weddell sector and moves over the Ellsworth Land before flowing
405 down the length of PIG drainage basin (Fig. 5b). The wavenumber #1 is maintained by both low-
406 latitude forcing (Quintanar and Mechoso 1995a and b) and the high topography of Antarctica
407 (Hoskins and Karoly, 1981). As noted by Pohl et al. (2010), the AAO has a strong correlation with
408 ENSO, with El Nino events favoring its negative phase. This mode dominates in the colder months
409 from May to August (Fig. 5e) when the ASL is displaced westwards (Raphael et al., 2016) and
410 hence the SAM has a smaller impact on the weather conditions at PIG.

411

412 The second cluster (Fig. 5c) corresponds to the positive phase of the SAM in which the storm
413 track is shifted poleward and the ASL is significantly deeper (Fogt and Marshall, 2020; Zheng and
414 Li, 2022). Mclennan and Lenaerts (2021) found that the ASL modulates the total annual snowfall
415 at the Thwaites Glacier adjacent to PIG (Fig. 1a). This cluster shows the winds descending the
416 slopes immediately to the east of the Pine Island ice shelf. The air mass comes from the Pacific
417 Ocean and flows over the high terrain and coastal mountains directly to the northeast of PIG before
418 descending downslope into the glacier basin (Fig. 5d). The cyclonic (clockwise) circulation motion
419 associated with the ASL, and its interaction with the high terrain to the east of PIG, leads to Foehn
420 conditions around the glacier. Cluster #2 features a wavenumber #3 across the Southern
421 Hemisphere.

422

423



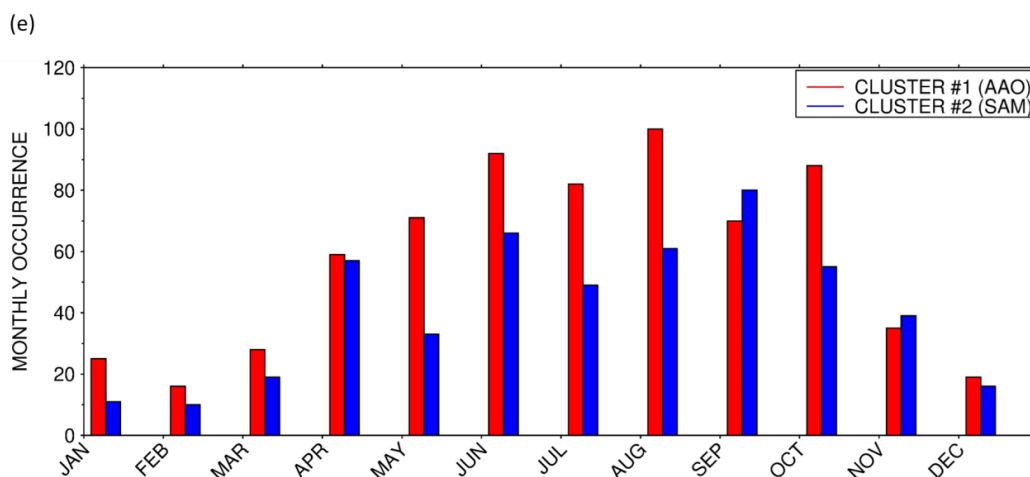


Figure 5: Large-scale conditions promoting Foehn events: (a) 200 hPa geopotential height anomalies (shading; m) and wind vectors (arrows; m s^{-1}) and (b) mean sea-level pressure (shading; hPa) and 10-m wind vectors (arrows; m s^{-1}) for cluster #1 of a k-means clustering technique applied to the daily-mean fields of 1181 Foehn days at PIG in 2000-2020. The cross gives the approximate location of PIG (100°W , $75^{\circ}10'\text{S}$). (c)-(d) are as (a)-(b) but for cluster #2. The monthly occurrence of each cluster is given in panel (e).

424 5. Illustrative Case Study: November 2011

425 The effects of Foehn at PIG are discussed for an event in November 2011. Fig. 6 summarises
426 the large-scale environment that promoted the occurrence of Foehn, while Fig. 7 presents a time-
427 series of spatially-averaged meteorological variables that allows for a quantification of the Foehn
428 effects.

429

430 The ASL was particularly deep on 10-11 November 2011, with the 500 hPa geopotential height
431 anomalies more than 1.5σ below the 1979-2020 mean (Figs. 6a-b). An atmospheric river
432 associated with an elongated and narrow band of high moisture content and integrated vapour
433 transport (IVT) values in the top 10% of the climatological distribution, extended from the
434 Southern Hemisphere mid-latitudes into West Antarctica and PIG, being transported by the
435 clockwise circulation of the ASL. As the ASL edged closer to the Antarctica Peninsula on 11
436 November (Fig. 6b), the more moist air, now over the Weddell Sea, penetrated further inland
437 reaching PIG and the surrounding region from the east (after flowing over the ice divide that
438 separates the Weddell Sea and Ronne Ice Shelf from PIG and the Amundsen Sea region). As a
439 result, the IVT at PIG more than doubled from about $27.5 \text{ kg m}^{-1} \text{ s}^{-1}$ on 10 November to around 65
440 $\text{ kg m}^{-1} \text{ s}^{-1}$ on 11 November, with the total column water vapour increasing to just under 4 kg m^{-2}
441 (Fig. 7a). The Foehn effect in this event corresponds to that of cluster #1 (Fig. 4a), the more indirect
442 pathway from the Weddell Sea as opposed to Foehn events triggered by Pacific warm air intrusions
443 (cluster #2, Fig. 4b).



444

445 As seen in Figs. 6c-d, the air mass accelerated downslope as it descended the mountains towards
446 coastal West Antarctica, with 10-m wind speeds higher than 20 m s^{-1} and in the top 10% of the
447 climatological distribution over a vast region including PIG (locally in the top 1% just to the
448 northwest and southeast of PIG), and downward sensible heat fluxes in excess of 75 W m^{-2} at PIG
449 (the negative, or upward pointing, fluxes around 75°S and 110°W are associated with a sea ice-
450 free area). These tendencies are seen in the area-averaged time-series (Fig. 7c) with the negative
451 (upward) latent heat flux indicating sublimation peaking on 11 November (Fig. 7f). In fact, the
452 phase of the latent heat flux matches that of the surface sublimation given in Fig. 7f. The opposite
453 sign of the sensible and latent heat fluxes, which roughly offset each other, is expected during
454 Foehn events (Elvidge et al., 2020), as the positive latent heat flux which arises due to sublimation
455 is opposed by the downward sensible heat flux due to the higher air than surface temperature. The
456 surface mass balance is essentially controlled by the surface and blowing snow sublimation, with
457 the precipitation/snowfall and the divergence terms playing a secondary role, and with the snow
458 melting being zero throughout the full period (Fig. 7f). The estimated maximum sublimation rate
459 is seen at the end of 10 November and has a magnitude of $\sim 0.13 \text{ mm w.e. hr}^{-1}$, comparable to the
460 ice loss due to ocean dynamics (e.g., Holland et al., 2007; Rintoul et al., 2016; Feldmann et al.,
461 2019) albeit in a non-sustained way. The ERA-5 snow depth, which accounts only for sublimation
462 and changes in snow density (snow melt is not simulated by ERA-5 during this event, Fig. 7f),
463 shows a steady decrease starting on 04 November and a faster drop from 11-13 November (not
464 shown). Besides sublimation, melting was detected in the Moderate Resolution Imaging
465 Spectroradiometer (MODIS; Kaufman et al., 1997) satellite imagery reaching a maximum on 12
466 November (Fig. 7g). The melting area at times exceeded $\sim 100 \text{ km}^2$ or roughly 2% of the central
467 trunk of the glacier (Wingham et al., 2009). The fact that ERA-5 does not simulate the observed
468 melting can be attributed to the way snow melting is parameterized in the model used to generate
469 the reanalysis dataset, only taking place if the temperature of the snow layer exceeds the melting
470 point (ECMWF, 2016), with ERA-5 exhibiting a cold bias over the high terrain in Antarctica (e.g.
471 Gonzalez et al., 2021). The observed melting area is also much smaller than ERA-5's spatial
472 resolution ($\sim 27 \text{ km} \times 27 \text{ km}$).

473

474 In Figs. 7d-e, the net shortwave, longwave and radiation fluxes from the reanalysis data are
475 compared with those estimated from satellite data, as given by the Clouds and Earth's Radiant
476 Energy System (CERES) SYN1deg dataset (Doelling et al. 2013, 2016). ERA-5 under-predicts
477 the net shortwave radiation flux during the day by up to a factor of 2.5, and the net longwave
478 radiation flux at night by up to 25 W m^{-2} . These differences are consistent with those reported by
479 Ghiz et al. (2021), who attributed the lower shortwave fluxes in ERA-5 compared to CERES to
480 differences in the cloud properties, with the reanalysis fluxes being more consistent with those
481 measured in situ at a site in the West Antarctic Ice Sheet than those of CERES. On the other hand,
482 CERES partially corrects the tendency of ERA-5 to under-predict the net longwave radiation flux
483 over Antarctica, in particular in clear-sky conditions (Silbert et al., 2019). During the November



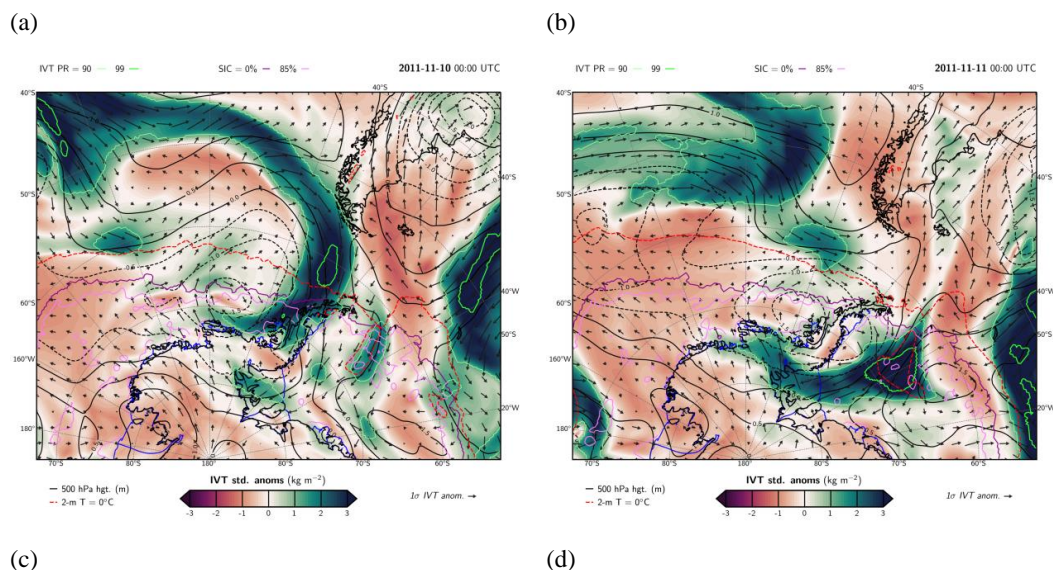
484 Foehn event, the area-averaged surface energy flux, F_{net} , is positive (Fig. 7e), as the positive
485 sensible heat flux offsets the negative latent heat flux (Fig. 7c), and the surface net shortwave
486 radiation flux overwhelms the negative net longwave flux (Fig. 7d). This indicates an excess of
487 energy towards the surface leading to snow melt and evaporation. The 3-5°C increase in air
488 temperature (Fig. 7b) with respect to the previous non-Foehn days, present both in the reanalysis
489 and weather station data, is comparable to that seen during a Foehn event at the Ross Ice Shelf in
490 January 2016 (Zou et al., 2019). Note that the ERA-5 values are area-averaged over the red box in
491 Fig. 1a and hence the fields are likely larger in local areas.

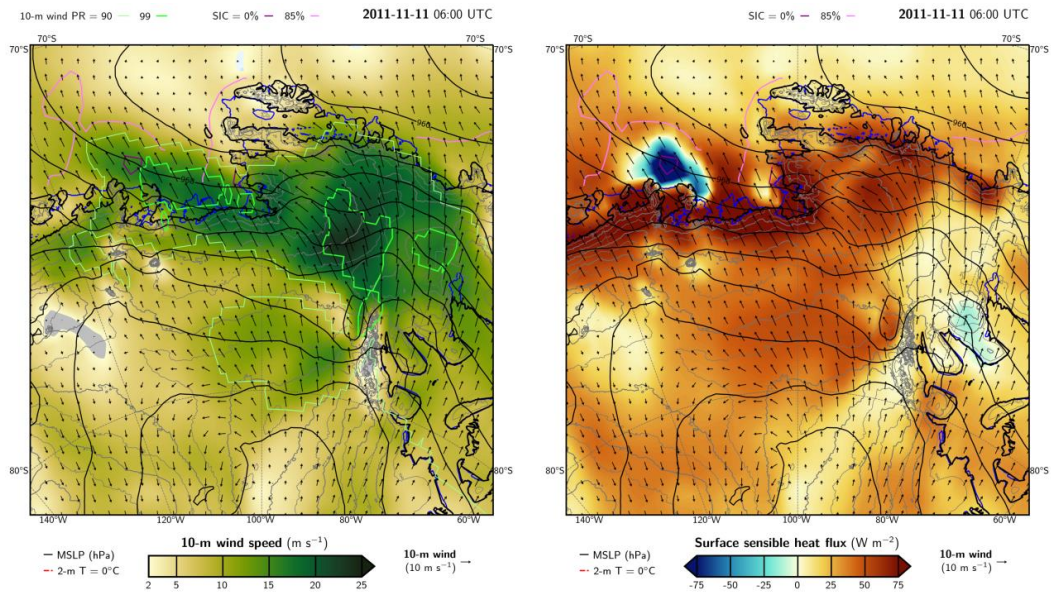
492

493 The Foehn event can also be seen in the Hovmoeller plots in Fig. 6e. The wind direction shifts
494 from northeast to southeast on 08-09 November 2011 around PIG as the ASL moves closer to the
495 Antarctica Peninsula. This is accompanied by an increase in the sensible heat flux, with a
496 latitudinally-averaged value exceeding 50 W m^{-2} that corresponds to an anomaly of about 40 W m^{-2} .
497 The fact that the peak in wind speed takes place $\sim 90^\circ\text{W}$ but that in the heat fluxes around 100° -
498 110°W is consistent with the warming of the air mass as it descends the slopes of the mountains
499 over West Antarctica. The drying of the atmosphere in association with the Foehn effects is also
500 present, with the RH dropping below 70% during the event. The sensible heat flux shows a clear
501 diurnal cycle, peaking around 05-06 UTC, which is roughly 00 Local Time (LT) for a longitude of
502 $\sim 100^\circ\text{W}$, out-of-phase with the surface radiation fluxes (Figs. 7c-e). This mismatch is also seen on
503 other days, and may be attributed to the effects of Foehn, clouds and moisture on the heat fluxes.
504 Weaker Foehn events, with peak wind speeds roughly half of that on 09-11 November but similar
505 values of RH, took place earlier in the month, on 03-04 November 2011.

506

507





(e)

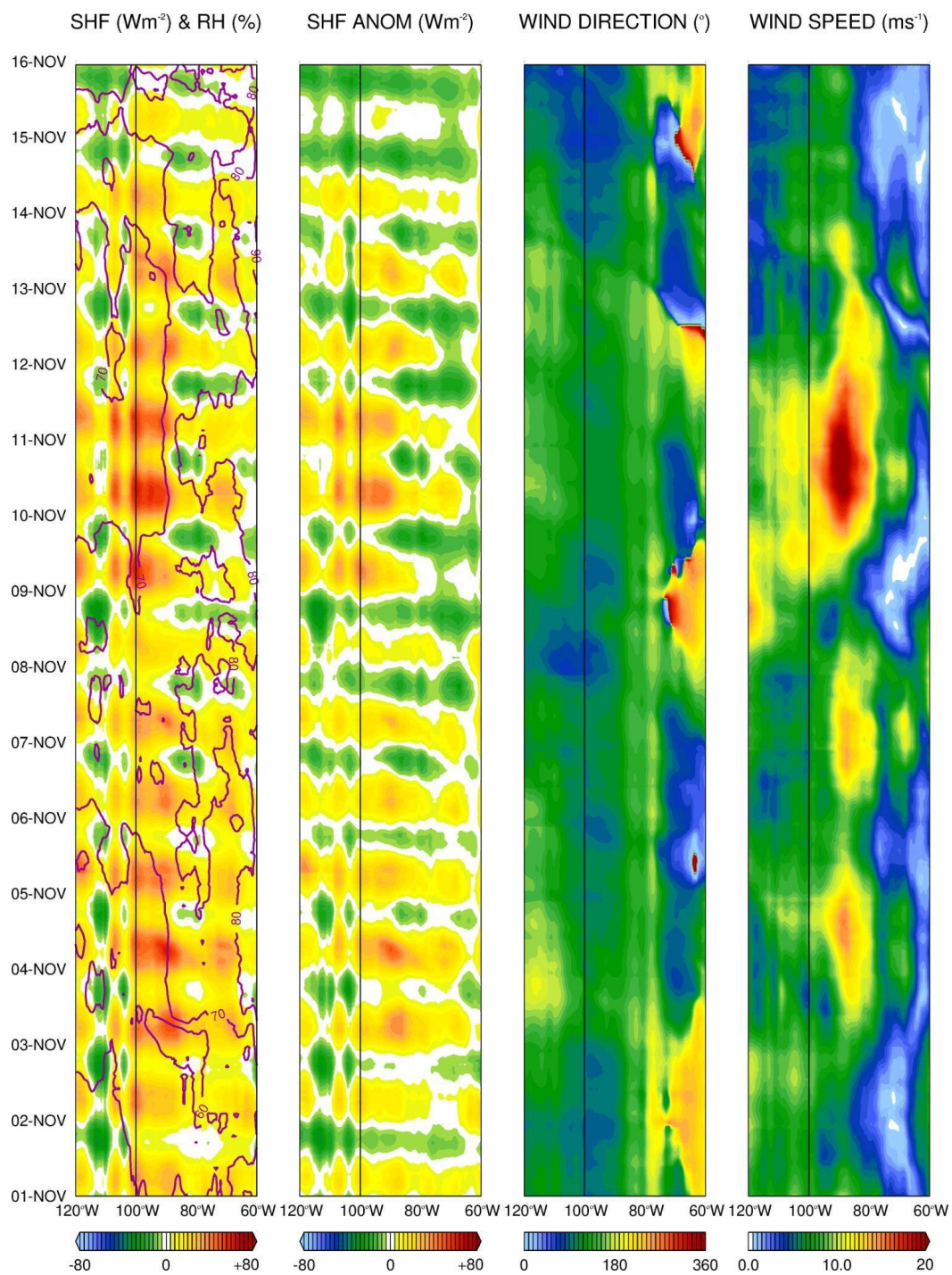




Figure 6: November 2011 Foehn events: Integrated Water Vapour Transport (IVT; kg m^{-2} ; shading) normalised anomalies with respect to ERA-5's 1979-2020 monthly climatology, one standard deviation anomaly is plotted as vectors, and 500 hPa geopotential height (m; contours) on (a) 10 November and (b) 11 November 2011 at 00 UTC. The thin and thick green lines denote the 90th and 99th IVT percentiles, respectively. (c) 10-m wind speed (shading; m s^{-1}), with the 90th and 99th percentiles denoted by the solid thin and thick green lines, respectively, mean sea-level pressure (solid black contours; hPa) and 10-m winds (vectors; m s^{-1}) on 11 November 2011 at 06 UTC. The grey lines are orographic contours drawn every 500 m. (d) is as (c) but with the shading giving the sensible heat flux (shading; W m^{-2}), positive if downwards towards the surface. In panels (a)-(d), the red dashed line is the 0°C 2-m temperature isotherm, and the dark solid purple and pink lines highlight regions where the sea-ice concentration is equal to 0% and 85%, respectively. The anomalies and percentile ranks for the IVT, 10-m horizontal winds, 500 hPa geopotential height and 2-m temperature are calculated from the distribution of all 3-h values within ± 15 Julian days from the given date during the 1979–2020 period and at a given grid point. (e) Hovmoeller plot of sensible heat flux (shading; W m^{-2}) and relative humidity (contours, every 10%), sensible heat flux anomalies with respect to the 1979-2021 climatology (W m^{-2}), and 10-m wind direction ($^{\circ}$) and speed (m s^{-1}) for 01-15 November 2011. The fields are averaged over 72.5°-77.5°S and are plotted for the region 120°W-60°W. All colour bars are linear with only the lowest, middle and highest values shown. The black vertical line indicates the approximate longitude of PIG (100°W).

508

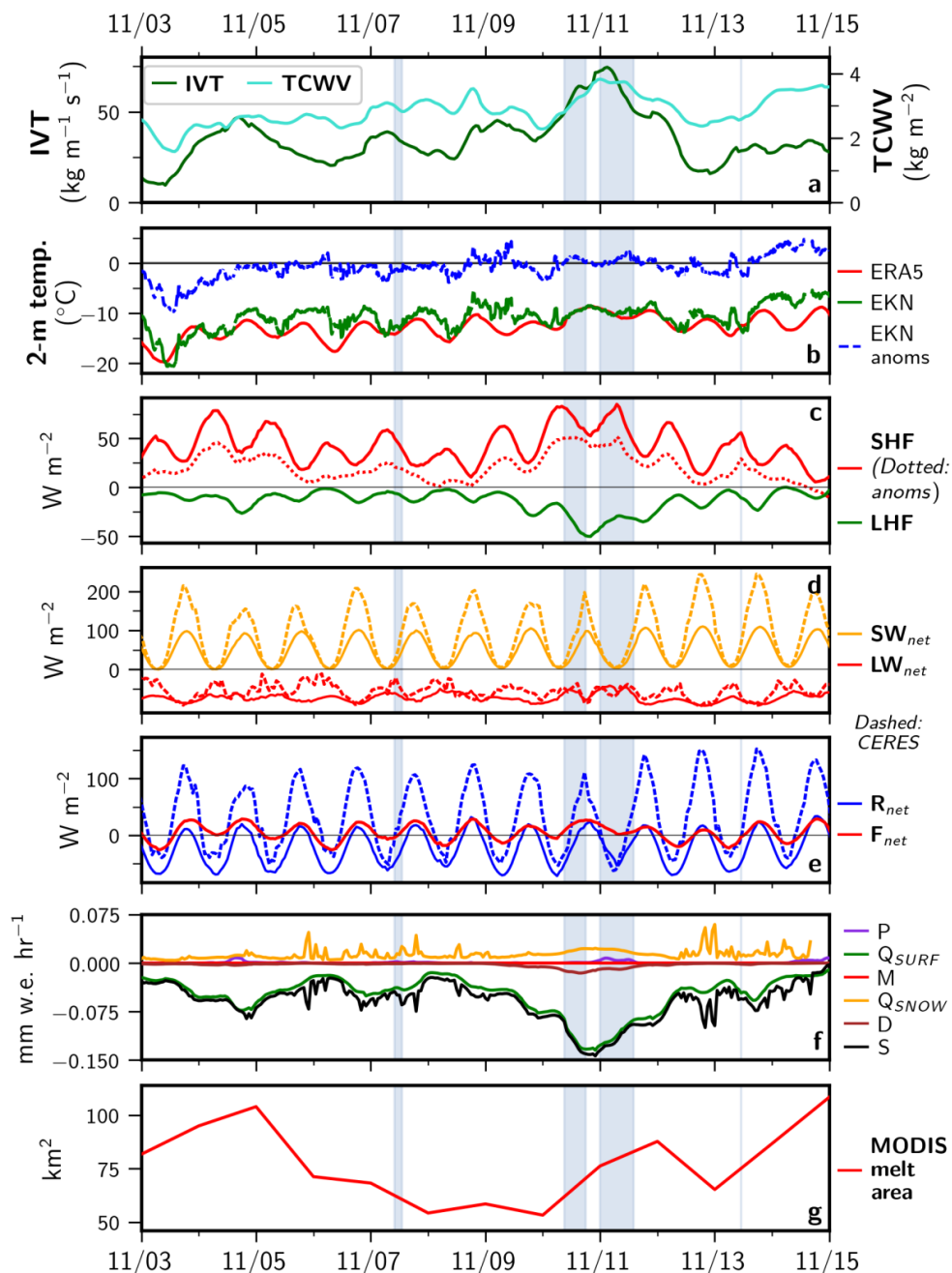


Figure 7: Impacts of Foehn winds on ice: Time series of 1-hourly ERA-5 variables averaged over PIG (red box in Fig. 1a) from 03 to 14 November 2011: (a) Integrated water vapor transport (IVT; light green; $\text{kg m}^{-1} \text{s}^{-1}$) and total column water vapor (TCWV; dark green; kg m^{-2}); (b) 10-min observed 2-m temperature (green; $^{\circ}\text{C}$) at the Evans Knoll weather station (-74.85°S , -100.404°W ; 188 m above sea-level), the anomalies with respect to the 2011–2015



hourly climatology are given by the dashed blue line, and area-averaged ERA-5 2-m temperature (red; °C); (c) ERA-5 sensible heat flux (SHF ; red; $W m^{-2}$) and latent heat flux (LHF ; orange; $W m^{-2}$); (d) net shortwave radiation (SW_{net} ; orange; $W m^{-2}$) and longwave radiation (LW_{net} ; red; $W m^{-2}$) flux at the surface; (e) net radiation (R_{net} ; blue; $W m^{-2}$) and total energy flux ($F_{net} = SHF + LHF + R_{net}$; red; $W m^{-2}$) at the surface; (f) individual components of the surface mass balance, Eq. (2), expressed in mm w.e. hr^{-1} . The S , P , M , Q_{surf} , Q_{snow} and D terms are given by the black, purple, red, green, orange and brown lines, respectively; (g) Daily total surface area (km^2) of melt ponds observed from MODIS imagery. In panel (c), the SHF anomalies, calculated as the difference from the domain-averaged 1979-2020 November hourly monthly mean, are also plotted. In (d)-(e), the net radiative variables from CERES averaged over the same domain are plotted as dashed lines for comparison. Times when Foehn occurred are shaded in blue.

509 6. Discussion and Conclusions

510 Pine Island Glacier (PIG), located in West Antarctica around 75°S and 100°W between the
511 Antarctic Peninsula to the east and the Ross Ice Shelf to the west, has been losing ice mass at an
512 accelerated rate over the last two decades. While the vast majority of the studies on ice loss at PIG
513 focus on ocean dynamics (e.g. Stanton et al., 2013; Favier et al., 2014), atmospheric forcing is also
514 likely to be important, with warmer and more moist air intrusions from the mid-latitudes and Foehn
515 effects the likely candidates (Ghiz et al., 2021). The role of moist air intrusions is well documented
516 (e.g. Willie et al., 2021), but less attention has been paid to Foehn, in particular around PIG where
517 the complex terrain promotes its occurrence. Foehn effects can lead to ice loss through
518 sublimation, which is typically a small-scale and invisible phenomenon in nature and hence
519 difficult to be detected using satellite data. At the same time, Foehn plays an important role in the
520 surface mass balance around Antarctica (Ghiz et al., 2021), and a better understanding of its
521 occurrence may help to reduce the major uncertainties that still exist (The IMBIE team, 2018). In
522 this work, a 41-year climatology of Foehn events at PIG is generated using ERA-5 reanalysis data,
523 and its impact on the surface mass balance is analyzed. The large-scale atmospheric circulation
524 patterns that favor Foehn events at PIG are also identified.

525

526 Foehn events at PIG are more frequent in the colder months from June to October, with an
527 average of 3.0 events per month in the 105°-95°W and 70°-80°S region in August 1980-2020 and
528 just 0.37 in January. The peak in austral winter is consistent with the poleward position of the mid-
529 latitude storm track, with the Amundsen Sea Low (ASL), a semi-permanent low pressure in the
530 Amundsen-Bellingshausen Seas, closest to the Antarctica coast in late winter. The presence of a
531 low just north of PIG favours easterly to southeasterly winds at the site, which encourages the
532 occurrence of Foehn. The duration of Foehn events exhibits a less pronounced annual cycle, with
533 Foehn episodes typically lasting 5 to 9 h. Both the number and duration of Foehn events at PIG are
534 smaller than those at other sites around Antarctica such as the Antarctic Peninsula, due to the
535 reduced exposure to the mid-latitude baroclinic systems.

536

537 The negative phase of the Antarctic Oscillation, in particular in the cold season (May to August),
538 and the positive phase of the Southern Annular Mode, foster the occurrence of Foehn at PIG. The
539 former is a more indirect pathway, with the air flow coming from the Weddell sector and moving



540 over the Ellsworth Land before reaching PIG, while in the latter the air mass comes from the
541 Pacific Ocean and flows over the high terrain directly to the northeast of PIG before descending
542 into the glacier basin. A trend analysis revealed that Foehn events have been occurring more
543 frequently (at a rate of about 4.1 days/41 years) in 1980-2020. There is, however, considerable
544 inter-annual variability, with the peaks generally coinciding with La Nina or neutral episodes,
545 while the lower values in El Nino events are associated with a weaker ASL.

546
547 A composite of Foehn and no-Foehn episodes revealed that Foehn events have an important impact
548 on the surface mass balance. It is concluded that surface sublimation plays the major role, with a
549 magnitude of ~ 1.434 mm water equivalent (w.e.) day^{-1} , comparable to that observed at other sites
550 in Antarctica. The blowing snow sublimation and divergence rate have a comparable magnitude
551 to that of the precipitation (snowfall) rate, with values of 0.35-0.36 mm w.e. day^{-1} . However, while
552 the former makes a positive contribution to the surface mass balance due to the convergence of the
553 snow transport rate at the glacier basin, the latter depletes surface snow, as the drier conditions
554 associated with Foehn reduce the likelihood of the occurrence of precipitation. The melting rate is
555 negligible and is restricted to the coastal areas to the north of the glacier.

556
557 A particularly strong Foehn event took place on 09-11 November 2011. During this period the
558 ASL was more than 1.5 standard deviations stronger than the 1979-2020 climatological mean, with
559 an atmospheric river from the Southeast Pacific injecting moisture into West Antarctica through
560 the Weddell Sea. As the southeasterly winds descended the high terrain east and southeast of the
561 glacier they accelerated, with 10-m wind speeds in excess of 20 m s^{-1} and in the top 10% of the
562 climatological distribution, and downward sensible heat fluxes higher than 75 W m^{-2} , a clear
563 signature of Foehn effects. Besides surface sublimation, at a rate of up to $0.13 \text{ mm w.e. hr}^{-1}$, melting
564 was detected using satellite data with the hourly melting area at times in excess of 100 km^2 .

565
566 As Foehn has been shown to play an important role in modulating ice conditions elsewhere
567 around Antarctica such as in the Antarctic Peninsula (Massom et al., 2018) and Ross Ice Shelf
568 (Zou et al. 2021a and b), a detailed analysis of Antarctica-wide Foehn occurrence is needed to
569 better quantify its contribution to snow sublimation and ice loss. The fact that Foehn winds are
570 more effective in inducing snow sublimation than snow melt, makes it challenging to detect their
571 total impact on the ice state at the scale of the continent as snow evaporation cannot be detected
572 from space. Advanced remote sensing techniques to detect changes in the depth of the snow layer
573 over land ice are therefore needed.

574 **Acknowledgment**

575 The authors wish to acknowledge the contribution of Khalifa University's high-performance
576 computing and research computing facilities to the results of this research. This work has been
577 supported by Masdar Abu Dhabi Future Energy Company through research grant number



578 8434000222. We also appreciate the support of the University of Wisconsin-Madison Automatic
579 Weather Station Program for the data set and information, NSF grant number 1924730.

580 **Code Availability**

581 The scripts used to process MODIS data and estimate the melting area are available upon request
582 from Dr. Catherine Walker (catherine.c.walker@nasa.gov). The codes used to estimate the terms
583 in the surface mass balance can be requested from Prof. Diana Francis (diana.francis@ku.ac.ae).

584 **Data Availability**

585 All the data used to generate the figures in this study has been uploaded to Francis et al. (2023).
586 ERA-5 hourly reanalysis surface (Hersbach et al. 2018b) and pressure-level (Hersbach et al.
587 2018a) data used in this work is freely available online on Copernicus' Climate Change Service
588 Climate Data Store website. The weather data for the Evans Knoll station located next to Pine
589 Island Glacier (PIG) is freely available at the Antarctic Meteorological Research Center &
590 Automatic Weather Stations Project website (Lazzara et al., 2022). The Antarctic 1 km Digital
591 Elevation Model (DEM) from Combined ERS-1 Radar and ICESat Laser Satellite Altimetry,
592 Version 1 (NSIDC-0422; Bamber et al. 2009a) used to plot Antarctica surface elevation,
593 MEaSUREs InSAR-Based Antarctica Ice Velocity Map, Version 2 (NSIDC-0484; Rignot et al.
594 2017) used to plot mean ice velocity of Pine Island and Thwaites Glaciers, and MEaSUREs
595 Antarctic Boundaries for IPY 2007-2009 from Satellite Radar, Version 2 (NSIDC-0709; Mougint
596 et al. 2017) are freely available available from the National Aeronautics and Space Administration
597 National Snow and Ice Data Center (NSIDC) Distributed Active Archive Center website. The
598 Clouds and Earth's Radiant Energy System (CERES) surface fluxes product SYN1deg - Level 3 has
599 been made publicly available at NASA/LARC/SD/ASDC (2017). Sentinel-2 satellite data, used to
600 extract the sea-ice front at PIG, is available online at (Copernicus, 2022). The MODIS daily global
601 surface reflectance Level 3 data (MOD09CMG, MYD09CMG; Vermote 2015a,b) are publicly
602 available from NASA Earthdata. The figures presented in this paper were generated using the
603 Interactive Data Language (IDL; Bowman, 2005) software version 8.8.1 and the Matplotlib
604 (Hunter, 2007) and Cartopy (Met Office, 2014) python libraries.

605 **Author Contribution**

606 DF conceived the study. RF and DF wrote the manuscript with inputs from KSM, SL and CW. SL
607 and CW processed the MODIS data while RF and KSM analyzed the reanalysis data. DF provided
608 formal analysis and validation of the results.
609

610 **Conflict of Interest**



611 SL is a member of the editorial board of The Cryosphere and this is handled according to the
612 journal policies.

613 **References**

614 Adusumilli, S., Fish, M. A., Fricker, H. and Medley, B. (2021) Atmospheric river precipitation contributed
615 to rapid increases in surface height of the West Antarctic Ice Sheet in 2019. *Geophysical Research Letters*,
616 48, e2020GL091076. <https://doi.org/10.1029/2020GL091076>.

617
618 Aulicino, G., Sansiviero, M., Paul, S., Cesarano, C., Fusco, G., Wadhams, P., Budillon, G. (2018) A New
619 Approach for Monitoring the Terra Nova Bay Polynya through MODIS Ice Surface Temperature Imagery
620 and Its Validation during 2011 and 2011 Winter Seasons. *Remote Sensing*, 10, 366.
621 <https://doi.org/10.3390/rs10030366>.

622
623 [Dataset] Bamber, J., Gomez-Dans, J. L. and Griggs, J. A. (2009a) Antarctic 1km Digital Elevation Model
624 (DEM) from Combined ERS-1 Radar and ICESat Laser Satellite Altimetry, version 1. Boulder, Colorado
625 USA. National Aeronautics and Space Administration National Snow and Ice Data Center Distributed
626 Active Archive Center. Accessed on 26 April 2022, available online at
627 <https://doi.org/10.5067/H0FQ1KL9NEKM>.

628
629 Bamber, J. L., Riva, R. E. M., Vermeersen, B. L. A. and LeBrocq, A. M. (2009b) Reassessment of the
630 potential sea-level rise from a collapse of the West Antarctic Ice Sheet. *Science*, 324, 901-903.
631 <https://doi.org/10.1126/science.1169335>.

632
633 Bell, R. E., Banwell, A. F., Trusel, L. D. and Kingslake, J. (2018) Antarctic surface hydrology and impacts
634 on ice-sheet mass balance. *Nature Climate Change*, 8, 1044-1052. <https://doi.org/10.1038/s41558-018-0326-3>.

635
636
637 Bowman, K. P. (2005) *An Introduction to Programming with IDL: Interactive Data Language [Software]*.
638 Academic Press, 304 pp., ISBN-10: 012088559X, ISBN-13: 978-0120885596.

639
640 Bozkurt, D., Rondanelli, R., Marin, J. C. and Garreaud, R. (2018) Foehn event triggered by an atmospheric
641 river underlies record-setting temperature along continental Antarctica. *Journal of Geophysical Research:*
642 *Atmospheres*, 123, 3871-3892. <https://doi.org/10.1002/2017JD027796>.

643
644 Bromwich, D. H. (1989) Satellite Analysis of Antarctic Katabatic Wind Behavior. *Bulletin of the American*
645 *Meteorological Society*, 70, 738-749. [https://doi.org/10.1175/1520-0477\(1989\)070<0738:SAOAKW>2.0.CO;2](https://doi.org/10.1175/1520-0477(1989)070<0738:SAOAKW>2.0.CO;2).

646
647
648 Cape, M. R., Vernet, M., Kahru, M. and Spreen, G. (2014) Polynya dynamics drive primary production in
649 the Larsen A and B embayments following ice-shelf collapse. *Journal of Geophysical Research: Oceans*,
650 119, 572-594. <https://doi.org/10.1002/2013JC009441>.

651



- 652 Cape, M. R., Vernet, M., Skvarca, P., Marinsek, S., Scambos, T. and Domack, E. (2015) Foehn winds link
653 climate-driven warming to ice shelf evolution in Antarctica. *Journal of Geophysical Research:*
654 *Atmospheres*, 120, 11037-11057. <https://doi.org/10.1002/2015JD023465>.
655
- 656 [Dataset] Copernicus (2022) Copernicus Open Access Hub. Available online at
657 <https://scihub.copernicus.eu/>, accessed on 10 October 2022.
658
- 659 Das, I., Bell, R. E., Scambos, T. A., Wolovick, M., Creyts, T. T., Studinger, M., Frearson, N., Nicolas, P.,
660 Lenaerts, J. T. M. and van den Broeke, M. (2013) Influence of persistent wind scour on the surface mass
661 balance of Antarctica. *Nature Geoscience*, 6, 367-371. <https://doi.org/10.1038/ngeo1766>.
662
- 663 Datta, R. T., Tedesco, M., Fettweis, X., Agosta, C., Lhermitte, S., Lenaerts, J. T. M., Wever, N. (2019) The
664 effect of Foehn-induced surface melt on firn evolution over the northeast Antarctic peninsula. *Geophysical*
665 *Research Letters*, 46, 3822-3831. <https://doi.org/10.1029/2018GL080845>.
666
- 667 De Rydt, J., Reese, R., Paolo, F. S. and Gudmundsson, G. H. (2021) Drivers of Pine Island Glacier speed-
668 up between 1996 and 2016. *The Cryosphere*, 15, 113-132. <https://doi.org/10.5194/tc-15-113-2021>.
669
- 670 Dery, S. J., Yau, M. K. (1999) A Bulk Blowing Snow Model. *Boundary-Layer Meteorology*, 93, 237-251.
671 <https://doi.org/10.1023/A:1002065615856>.
672
- 673 Dery, S. J., Yau, M. K. (2002) Large-scale mass balance effects of blowing snow and surface sublimation.
674 *Journal of Geophysical Research*, 107, 4679. <https://doi.org/10.1029/2001JD001251>.
675
- 676 Dias da Silva, P. E., Hodges, K. I., Coutinho, M. M. (2021) How well does the HadGEM2-ES coupled
677 model represent the Southern Hemisphere storm tracks? *Climate Dynamics*, 56, 1145-1162.
678 <https://doi.org/10.1007/s00382-020-05523-9>.
679
- 680 Dirscherl, M. C., Dietz, A. J., Kuenzer, C. (2021) Seasonal evolution of Antarctic supraglacial lakes in
681 2015-2021 and links to environmental controls. *The Cryosphere*, 15, 5205-5226. [https://doi.org/10.5194/tc-](https://doi.org/10.5194/tc-15-5205-2021)
682 [15-5205-2021](https://doi.org/10.5194/tc-15-5205-2021).
683
- 684 Djoumna, G. and Holland, D. M. (2021) Atmospheric rivers, warm air intrusions, and surface radiation
685 balance in the Amundsen Sea Embayment. *Journal of Geophysical Research: Atmospheres*, 126,
686 e2020JD034119. <https://doi.org/10.1029/2020JD034119>.
687
- 688 Doelling, D. R., Loeb, N. G., Keyes, D. F., Nordeen, M. L., Morstad, D., Nguyen, C., Wielicki, B. A.,
689 Young, D. F. and Sun, M. (2013) Geostationary Enhanced Temporal Interpolation for CERES Flux
690 Products. *Journal of Atmospheric and Oceanic Technology*, 30, 1072-1090.
691 <https://doi.org/10.1175/JTECH-D-12-00136.1>.
692
- 693 Doelling, D. R., Sun, M., Nguyen, L. T., Nordeen, M. L., Haney, C. O., Keyes, D. F. and Mlynczak, P. E.
694 (2016) Advances in Geostationary-Derived Longwave Fluxes for the CERES Synoptic (SYN1deg) Product.



- 695 Journal of Atmospheric and Oceanic Technology, 33(3), 503-521. [https://doi.org/10.1175/JTECH-D-15-](https://doi.org/10.1175/JTECH-D-15-0147.1)
696 [0147.1](https://doi.org/10.1175/JTECH-D-15-0147.1).
697
698 Donat-Magnin, M., Jourdain, N. C., Kittel, C., Agosta, C., Amory, C., Gallee, H., Kinner, G., Chekki, M.
699 (2021) Future surface mass balance and surface melt in the Amundsen sector of the West Antarctic Ice
700 Sheet. The Cryosphere, 15, 571-593. <https://doi.org/10.5194/tc-15-571-2021>.
701
702 ECMWF (2016) IF Documentation - Cy43r1 Operational Implementation 22 Nov 2016. Part IV: Physical
703 Processes. Accessed on 26 October 2022, available online at
704 <https://www.ecmwf.int/sites/default/files/elibrary/2016/17117-part-iv-physical-processes.pdf>.
705
706 Elvidge, A. D., Kuipers Munneke, P., King, J. C., Renfrew, I. A., Gilbert, E. (2020) Atmospheric drivers
707 of melt on Larsen C Ice Shelf: Surface energy budget regimes and the impact of foehn. Journal of
708 Geophysical Research: Atmospheres, 125, e2020JD032463. <https://doi.org/10.1029/2020JD032463>.
709
710 Elvidge, A. D. and Renfrew, I. A. (2016) The Causes of Foehn Warming in the Lee of Mountains. Bulletin
711 of the American Meteorological Society, 97(3), 455-466. <https://doi.org/10.1175/BAMS-D-14-00194.1>.
712
713 Elvidge, A. D., Renfrew, I. A., King, J. C., Orr, A., Lachlan-Cope, T. A. (2016) Foehn warming
714 distributions in nonlinear and linear flow regimes: a focus on the Antarctic Peninsula. Quarterly Journal of
715 the Royal Meteorological Society, 142, 618-631. <https://doi.org/10.1002/qj.2489>.
716
717 Favier, L., Durand, G., Cornford, S. L., Gudmundsson, G. H., Gagliardini, O., Gillet-Chaulet, F., Zwinger,
718 T., Payne, A. J. and Le Brocq, A. M. (2014) Retreat of Pine Island Glacier controlled by marine ice-sheet
719 instability. Nature Climate Change, 4, 117-121. <https://doi.org/10.1038/nclimate2094>.
720
721 Feldmann, J., Levermann, A., Mengel, M. (2019) Stabilizing the West Antarctic Ice Sheet by surface mass
722 deposition. Science Advances, 5. <https://doi.org/10.1126/sciadv.aaw4132>.
723
724 Fogt, R. L. and Marshall, G. J. (2020) The Southern Annular Mode: Variability, trends, and climate impacts
725 across the Southern Hemisphere. WIREs Climate Change, 11, e625. <https://doi.org/10.1002/wcc.652>.
726
727 Francis, D., Fonseca, R., Mattingly, K., Lhermitte, S. and Walker, C. (2023) Datasets for the publication
728 “Foehn Winds at Pine Island Glacier and its role in Ice Shelf Sublimation and Surface Melt” [Dataset].
729 Zenodo, <https://zenodo.org/record/7707591>.
730
731 Francis, D., Fonseca, R., Mattingly, K. S., Marsh, O. J., Lhermitte, S. and Cherif, C. (2022) Atmospheric
732 triggers of the Brunt Ice Shelf calving in February 2021. Journal of Geophysical Research: Atmospheres,
733 127, e2021JD036424. <https://doi.org/10.1029/2021JD036424>.
734
735 Francis, D., Mattingly, K. S., Lhermitte, S., Temimi, M. and Heil, P. (2021) Atmospheric extremes caused
736 high oceanward sea surface slope triggering the biggest calving event in more than 50 years at the Amery
737 Ice Shelf. The Cryosphere, 15, 2147-2165. <https://doi.org/10.5194/tc-15-2147-2021>.
738



- 739 Francis, D., Mattingly, K. S., Temimi, M., Massom, R. and Heil, P. (2020) On the crucial role of
740 atmospheric rivers in the two major Weddell Polynya events in 1973 and 2017 Antarctica. *Science*
741 *Advances*, 6, eabc2695. <https://doi.org/10.1126/sciadv.abc2695>.
742
- 743 Gehring, J., Vignon, E., Billaut-Roux, A.-C., Ferrone, A., Protat, A., Alexander, S. P., Berne, A. (2022)
744 Orographic flow influence on precipitation during an atmospheric river event at Davis, Antarctica. *Journal*
745 *of Geophysical Research: Atmospheres*, 127, e2021JD035210. <https://doi.org/10.1029/2021JD035210>.
746
- 747 Ghiz, M. K., Scott, R. C., Vogelmann, A. M., Lenaerts, J. T. M., Lazzara, M. and Lubin, D. (2021) Energetic
748 of surface melt in West Antarctica. *The Cryosphere*, 15, 3459-3494. [https://doi.org/10.5194/tc-15-3459-](https://doi.org/10.5194/tc-15-3459-2021)
749 [2021](https://doi.org/10.5194/tc-15-3459-2021).
750
- 751 Gong, D. and Wang, S. (1999) Definition of Antarctic oscillation index. *Geophysical Research Letters*,
752 26(4), 459-462. <https://doi.org/10.1029/1999GL900003>.
753
- 754 Gonzalez, S., Vasallo, F., Sanz, P., Quesada, A. and Justel, A. (2021) Characterization of the summer
755 surface mesoscale dynamics at Dome F, Antarctica. *Atmospheric Research*, 259, 105699.
756 <https://doi.org/10.1016/j.atmosres.2021.105699>.
757
- 758 Gorodetskaya, I. V., Kneifel, S., Maahn, M., Van Tricht, K., Thiery, W., Schween, J. H., Mangold, A.,
759 Crewell, S., Van Lipzig, N. P. M. (2015) Cloud and precipitation properties from ground-based remote-
760 sensing instruments in East Antarctica. *The Cryosphere*, 9, 285-304. <https://doi.org/10.5194/tc-9-285-2015>.
761
- 762 Gossart, A., Helsen, S., Lenaerts, J. T. M., Vanden Broucke, S., van Lipzig, N. P. M. and Souverijns, N.
763 (2019) An Evaluation of Surface Climatology in State-of-the-Art Reanalyses over the Antarctic Ice Sheet.
764 *Journal of Climate*, 32(20), 6899-6915. <https://doi.org/10.1175/JCLI-D-19-0030.1>.
765
- 766 Goyal, R., Jucker, M., Gupta, A. S., Hendon, H. H. and England, M. H. (2021) Zonal wave 3 pattern in the
767 Southern Hemisphere generated by tropical convection. *Nature Geosciences*, 14, 732-738.
768 <https://doi.org/10.1038/s41561-021-00811-3>.
769
- 770 Greene, C. A., Gardner, A. S., Schlegel, N.-J. and Fraser, A. D. (2022) Antarctic calving loss rivals ice-
771 shelf thinning. *Nature*, 609, 948-953. <https://doi.org/10.1038/s41586-022-050307-w>.
772
- 773 [Dataset] Hersbach, H., Bell, B., Berrisford, P., Biavati, G., Horanyi, A., Muñoz Sabater, J., Nicolas, J.,
774 Peubey, C., Radu, R., Rozum, I., Schepers, D., Simmons, A., Soci, C., Dee, D. and Thepaut, J.-N. (2018a)
775 ERA5 hourly data on pressure levels from 1959 to present. Copernicus Climate Change Service (C3S)
776 Climate Data Store (CDS). <https://doi.org/10.24381/cds.bd0915c6>.
777
- 778 [Dataset] Hersbach, H., Bell, B., Berrisford, P., Biavati, G., Horanyi, A., Muñoz Sabater, J., Nicolas, J.,
779 Peubey, C., Radu, R., Rozum, I., Schepers, D., Simmons, A., Soci, C., Dee, D. and Thepaut, J.-N. (2018b)
780 ERA5 hourly data on single levels from 1959 to present. Copernicus Climate Change Service (C3S) Climate
781 Data Store (CDS). <https://doi.org/10.24381/cds.adbb2d47>.
782



- 783 Hofsteenge, M. G., Cullen, N. J., Reijmer, C., van den Broeke, M., Katurji, M., Orwin, J. F. (2022) The
784 surface energy balance during foehn events at Joyce Glacier, McMurdo Dry Valleys, Antarctica. The
785 Cryosphere, 16, 5041-5059. <https://doi.org/10.5194/tc-16-5041-2022>.
786
- 787 Holland, P. R., Brisbourne, A., Corr, H. F. J., McGrath, D., Purdon, K., Paden, J., Fricker, H. A., Paolo, F.
788 S. and Fleming, A. H. (2015) Oceanic and atmospheric forcing of Larsen C Ice-Shelf thinning. The
789 Cryosphere, 9, 1005-1024. <https://doi.org/10.5194/tc-9-1005-2015>.
790
- 791 Holland, P. R., Feltham, D. L., Jenkins, A. (2007) Ice Shelf Water plume flow beneath Filchner-Ronne Ice
792 Shelf, Antarctica. Journal of Geophysical Research, 112, C05044. <https://doi.org/10.1029/2006JC003915>.
793
- 794 [Dataset] Hunter, J. D. (2007) Matplotlib: A 2D graphics environment . Computing in Science and
795 Engineering, 9, 90-95. <https://doi.org/10.1109/MSCE.2007.55>.
796
- 797 Hoskins, B. J. and Karoly, D. J. (1981) The Steady Linear Response of a Spherical Atmosphere to Thermal
798 and Orographic Forcing. Journal of Atmospheric Sciences, 38(6), 1179-1996. [https://doi.org/10.1175/1520-0469\(1981\)038<1179:TSLROA>2.0.CO;2](https://doi.org/10.1175/1520-0469(1981)038<1179:TSLROA>2.0.CO;2).
799
- 800
- 801 Jacobs, S., Jenkins, A., Giulivi, C. and Dutrieux, P. (2011) Stronger ocean circulation and increased melting
802 under Pine Island Glacier ice shelf. Nature Geosciences, 4, 519-523. <https://doi.org/10.1038/ngeo1188>.
803
- 804 Jenkins, A., Dutrieux, P., Jacobs, S. S., McPhail, S. D., Perrett, J. R., Webb, A. T. and White, D. (2010)
805 Observations beneath Pine Island Glacier in West Antarctica and implications for its retreat. Nature
806 Geosciences, 3, 468-472. <https://doi.org/10.1038/ngeo890>.
807
- 808 Joughin, I., Shapero, D., Smith, B., Dutrieux, P. and Barham, M. (2021) Ice-shelf retreat drives recent Pine
809 Island Glacier speedup. Science Advances, 7(24). <https://doi.org/10.1126/sciadv.abg3080>.
810
- 811 Kaufman, Y. J., Tanre, D., Rmer, L. A., Vermote, E. F., Chu, A. and Holben, B. N. (1997) Operational
812 remote sensing of tropospheric aerosol over land from EOS moderate resolution imaging spectroradiometer.
813 Journal of Geophysical Research, 192, 17051-17067. <https://doi.org/10.1029/96JD03988>.
814
- 815 Kirchgaessner, A., King, J. C. and Anderson, P. S. (2021) The impact of Fohn conditions across the
816 Antarctic Peninsula on local meteorology based on AWS measurements. Journal of Geophysical Research:
817 Atmospheres, 126, e2020JD033748. <https://doi.org/10.1029/2020JD033748>.
818
- 819 Kowalewski, S., Helm, V., Morris, E. M. and Eisen, O. (2021) The regional-scale surface mass balance of
820 Pine Island Glacier, West Antarctica, over the period 2005-2014, derived from airborne radar soundings
821 and neutron probe measurements. The Cryosphere, 15, 1285-1305. <https://doi.org/10.5194/tc-15-1285-201>.
822
- 823 Laffin, M. K., Zender, C. S., Singh, S., Van Wessem, J. M., Smeets, C. J. P. P. and Reijmer, C. H. (2021)
824 Climatology and evolution of the Antarctic Peninsula foehn wind-induced melt regime from 1979-2018.
825 Journal of Geophysical Research: Atmospheres, 126, e2020JD033682.
826 <https://doi.org/10.1029/2020JD033682>.



- 827
828 [Dataset] Lazzara, M. (2022) Antarctic Meteorological Research Center & Automatic Weather Stations
829 Project. Accessed on 06 November 2022, available online at <http://amrc.ssec.wisc.edu/>.
830
831 Lhermitte, S., Sun, S., Shuman, C., Wouters, B., Pattyn, F., Wuite, J., Berthier, E. and Nagler, T. (2021)
832 Damage accelerates ice shelf instability and mass loss in Amundsen Sea Embayment. Proceeding of the
833 National Academy of Sciences of the United States of America, 117(40), 24735-24741.
834 <https://doi.org/10.1073/pnas.1912890117>.
835
836 Lestari, R. K. and Koh, T.-Y. (2016) Statistical Evidence for Asymmetry in ENSO-IOD Interactions.
837 Atmosphere-Ocean, 54(5), 498-504. <https://doi.org/10.1080/07055900.2016.1211084>.
838
839 Li, S., Liao, J. and Zhang, L. (2022) Extraction and analysis of elevation changes in Antarctic ice sheet
840 from CryoSat-2 and Sentinel-3 radar altimeters. Journal of Applied Remote Sensing, 16(3), 034514.
841 <https://doi.org/10.1117/1.JRS.16.034514>.
842
843 Liu, S., Su, S., Cheng, Y., Tong, X. and Li, R. (2022) Long-Term Monitoring and Change Analysis of Pine
844 Island Ice Shelf Based on Multi-Source Satellite Observations during 1973-2020. Journal of Marine Science
845 and Engineering, 10, 976. <https://doi.org/10.3390/jmse10070976>.
846
847 Marshall, G. J. (2003) Trends in the Southern Annular Mode from observations and reanalyses. Journal of
848 Climate, 16, 4134-4143. [https://doi.org/10.1175/1520-0442\(2003\)16<4134:3ATITSAM>2.0.CO;2](https://doi.org/10.1175/1520-0442(2003)16<4134:3ATITSAM>2.0.CO;2).
849
850
851 Massom, R. A., Scambos, T. A., Bennetts, L. K., Reid, P., Squire, V. A. and Stammerjohn, S. E. (2018)
852 Antarctic ice shelf disintegration triggered by sea ice loss and ocean swell. Nature, 558, 383-389.
853 <https://doi.org/10.1038/s41586-018-0212-1>.
854
855 MacDonald, M. K., Pomeroy, J. W., Essery, R. L. H. (2018) Water and energy fluxes over northern prairies
856 as affected by chinook winds and winter precipitation. Agricultural and Forest Meteorology, 248, 372-385.
857 <https://doi.org/10.1016/j.agrformet.2017.10.025>.
858
859 McLennan, M. L. and Lenaerts, J. T. M. (2021) Large-scale atmospheric drivers of snowfall over Thwaites
860 Glacier, Antarctica. Geophysical Research Letters, 48, e2021GL093644.
861 <https://doi.org/10.1029/2021GL093644>.
862
863 [Dataset] Met Office (2014) Cartopy: a cartographic python library with a Matplotlib interface. Accessed
864 on 29 June 2022, available online at <https://scitools.org.uk/cartopy>.
865
866 Meredith, M. P., Inall, M. E., Brearley, J. A., Ehmen, T., Sheen, K., Munday, D., Cook, A., Retallick, K.,
867 Van Landeghem, K., Gerrish, L., Annett, A., Carvalho, F., Jones, R., Gabarato, A. C. N., Bull, C. S., Wallis,
868 B. J., Hogg, A. E. and Scourse, J. (2022) Internal tsunamigenesis and ocean mixing driven by glacier calving
869 in Antarctica. Science Advances, 8(47). <https://doi.org/10.1126/sciadv.add0720>.
870



- 871 Miles, B. W. J., Stokes, C. R. and Jamieson, S. S. R. (2017) Simultaneous disintegration of outlet glaciers
872 in Porpoise Bay (Wilkes Land), East Antarctica, driven by sea ice break-up. *The Cryosphere*, 11, 427-442.
873 <https://doi.org/10.5194/tc-11-427-2017>.
874
- 875 Moncada, J. M. and Holland, D. M. (2019) Automatic Weather Station Pine Island Glacier. United States
876 Antarctic Program (USAP) Data Center. Accessed on 26 April 2022, <https://doi.org/10.15784/601216>.
877
- 878 Montesi, J., Elder, K., Schmidt, R. A., David, R. E. (2004) Sublimation of Intercepted Snow within a
879 Subalpine Forest Canopy at Two Elevations. *Journal of Hydrometeorology*, 5, 763-773.
880 [https://doi.org/10.1175/1525-7541\(2004\)005<0763:SOISWA>2.0.CO;2](https://doi.org/10.1175/1525-7541(2004)005<0763:SOISWA>2.0.CO;2).
881
- 882 Mottram, R., Hansen, N., Kittel, C., van Wessem, J. M., Agosta, C., Amory, C., Boberg, F., van de Berg,
883 W., Fettweis, X., Gossart, A., van Lipzig, N. P. M., van Meijgaard, E., Orr, A., Phillips, T., Webster, S.,
884 Simonsen, S. B. and Souverijns, N. (2021) What is the surface mass balance of Antarctica? An
885 intercomparison of regional climate model estimates. *The Cryosphere*, 15, 3751-3784.
886 <https://doi.org/10.5194/tc-15-3751-2021>.
887
- 888 [Dataset] Mougnot, J., B. Scheuchl, and E. Rignot. 2017. MEaSUREs Antarctic Boundaries for IPY 2007-
889 2009 from Satellite Radar, Version 2. Boulder, Colorado USA. NASA National Snow and Ice Data Center
890 Distributed Active Archive Center. <https://doi.org/10.5067/AXE4121732AD>. Accessed on 8 November
891 2022.
892
- 893 Moussavi, M. S., Abdalati, W., Pope, A., Scambos, T., Tedesco, M., MacFerrin, M. and Grigsby, S. (2016)
894 Derivation and validation of supraglacial lake volumes on the Greenland Ice Sheet from high-resolution
895 satellite imagery. *Remote Sensing of Environment*, 183, 294-303.
896 <https://doi.org/10.1016/j.rse.2016.05.024>.
897
- 898 [Dataset] NASA (National Aeronautics and Space Administration) / LARC (Langley Research Center) /
899 SD (Science Division) / ASDC (Atmospheric Data Center) (2017) CERES and GEO-Enhanced TOA,
900 Within-Atmosphere and Surface Fluxes, Clouds and Aerosols 1-Hourly Terra-Aqua Edition4A. NASA
901 Langley Atmospheric Science Data Center DAAC. Retrieved from
902 https://doi.org/10.5067/TERRA+AQUA/CERES/SYN1DEG-1HOUR_L3.004A.
903
- 904 Nilsson, J., Gardner, A. S. and Paolo, F. S. (2022) Elevation change of the Antarctic Ice Sheet: 1985 to
905 2020. *Earth System Science Data*, 14, 3573-3598. <https://doi.org/10.5194/essd-14-3573-2022>.
906
- 907 Orr, A., Deb, P., Clem, K. R., Gilbert, E., Bromwich, D. H., Boberg, F., Colwell, S., Hansen, N., Lazzara,
908 M. A., Mooney, P. A., Mottram, R., Niwano, M., Phillips, T., Pishniak, D., Reijmer, C. H., van de Berg,
909 W. J., Webster, S. and Zuo, X. (2022) Characteristics of surface “melt potential” over Antarctic ice shelves
910 based on regional atmospheric model simulations of summer air temperature extremes from 1979/80 to
911 2018/19. *Journal of Climate*, 1-61. <https://doi.org/10.1175/JCLI-D-22-0386.1>.
912



- 913 Pohl, B., Fauchereau, N., Reason, C. J. C. and Rouault, M. (2010) Relationships between the Antarctic
914 Oscillation, the Madden-Julian Oscillation, and ENSO, and Consequences for Rainfall Analysis. *Journal of*
915 *Climate*, 23(2), 238-254. <https://doi.org/10.1175/2009JCLI2443.1>.
916
- 917 Polvani, L. M., Banerjee, A., Chemke, R., Doddridge, E. W., Ferreira, D., Gnanadesikan, A., Holland, M.
918 A., Kostov, Y., Marshall, J., Seviour, W. J. M., Solomon, S. and Waugh, D. W. (2021) Interannual SAM
919 modulation of Antarctic sea ice extent does not account for its long-term trends, pointing to a limited role
920 for ozone depletion. *Geophysical Research Letters*, 48, e2021GL098471.
921 <https://doi.org/10.1029/2021GL094871>.
922
- 923 Ponti, S., Scipionotti, R., Pierattini, S., Guglielmin, M. (2021) The Spatio-Temporal Variability of Frost
924 Blisters in a Perennial Frozen Lake along the Antarctic Coast as Indicator of the Goundwater Supply.
925 *Remote Sensing*, 13, 435. <https://doi.org/10.3390/rs13030435>.
926
- 927 Pradhananga, D., Pomeroy, J. W. (2022) Diagnosing changes in glacier hydrology from physical principles
928 using a hydrological model with snow redistribution, sublimation, firnification and energy balance ablation
929 algorithms. *Journal of Hydrology*, 608, 127545. <https://doi.org/10.1016/j.jhydrol.2022.127545>.
930
- 931 Quintanar, A. I. and Mechoso, C. R. (1995a) Quasi-Stationary Waves in the Southern Hemisphere. Part I:
932 Observational Data. *Journal of Climate*, 8(11), 2659-2672. [https://doi.org/10.1175/1520-
933 0442\(1995\)008<2659:QSWITS>2.0.CO;2](https://doi.org/10.1175/1520-0442(1995)008<2659:QSWITS>2.0.CO;2).
934
- 935 Quintanar, A. I. and Mechoso, C. R. (1995b) Quasi-Stationary Waves in the Southern Hemisphere. Part II:
936 Generation Mechanisms. *Journal of Climate*, 8(11), 2673-2690. [https://doi.org/10.1175/1520-
937 0442\(1995\)008<2673:QSWITS>2.0.CO;2](https://doi.org/10.1175/1520-0442(1995)008<2673:QSWITS>2.0.CO;2).
938
- 939 Raphael, M. N., Marshall, G. J., Turner, J., Fogt, R. L., Schneider, D., Dixon, D. A., Hosking, J. S., Jones,
940 J. M. and Hobbs, W. R. (2016) The Amundsen Sea Low: Variability, Change, and Impact on Antarctic
941 Climate. *Bulletin of the American Meteorological Society*, 97(1), 111-121. [https://doi.org/10.1175/BAMS-
942 D-14-00018.1](https://doi.org/10.1175/BAMS-D-14-00018.1).
943
- 944 Reijmer, C., Greuell, W. and Oerlemans, J. (1999) The annual cycle of meteorological variables and the
945 surface energy balance on Berkner Island, Antarctica. *Annals of Glaciology*, 29, 49-54.
946 <https://doi.org/10.3189/172756499781821166>.
947
- 948 [Dataset] Rignot, E., Mouginot, J. and Scheuchl, B. (2017) MEaSURES InSAR-Based Antarctica Ice
949 Velocity Map, Version 2. Boulder, Colorado USA. National Aeronautics and Space Administration
950 National Snow and Ice Data Center Distributed Active Archive Center. Accessed on 26 April 2022,
951 available online at <https://doi.org/10.5067/D7GK8F5J8M8R>.
952
- 953 Rintoul, S. R., Silvano, A., Pena-Molino, B., Wijk, E. V., Rosenberg, M., Geenbaum, J. E., Blankenship,
954 D. (2016) Ocean heat drives rapid basal melt of the Totten Ice Shelf. *Science Advances*, 2.
955 <https://doi.org/10.1126/sciadv.1601610>.
956



- 957 Rogers, R. R., Yau, M. K. (1989) A Short Course in Cloud Physics, 3rd edition. Pergamon, New York, 293
958 pp.
959
- 960 Rosier, S. H. R., Reese, R., Donges, J. F., De Rydt, J., Gudmundsson, G. H. and Winkelmann, R. (2021)
961 The tipping points and early warning indicators for Pine Island Glacier, West Antarctica. The Cryosphere,
962 15, 1501-1516. <https://doi.org/10.5194/tc-15-1501-2021>.
963
- 964 Rousseux, P. J. (1987) Silhouettes: A graphical aid to the interpretation and validation of cluster analysis.
965 Journal of Computational and Applied Mathematics, 20, 53-65. [https://doi.org/10.1016/0377-](https://doi.org/10.1016/0377-0427(87)90125-7)
966 [0427\(87\)90125-7](https://doi.org/10.1016/0377-0427(87)90125-7).
967
- 968 Scarchilli, C., Frezzotti, M., Grigioni, P., De Silvestri, L., Agnoletto, L., Dolci, S. (2010) Extraordinary
969 blowing snow transport events in East Antarctica. Climate Dynamics, 34, 1195-1206.
970 <https://doi.org/10.1007/s00382-009-0601-0>.
971
- 972 Scott, R. C., Nicolas, J. P., Bromwich, D. H., Norris, J. R. and Lubin, D. (2019) Meteorological Drivers
973 and Large-Scale Climate Forcing of West Antarctic Surface Melt. Journal of Climate, 32(3), 665-684.
974 <https://doi.org/10.1175/JCLI-D-18-0233.1>.
975
- 976 Silber, I., Verlinde, J., Wang, S.-H., Bromwich, D. H., Fridlind, A. M., Cadetdu, M., Eloranta, E. W. and
977 Flynn, C. J. (2019) Cloud Influence on ERA5 and AMPS Surface Downwelling Longwave Radiation Biases
978 in West Antarctica. Journal of Climate, 32(22), 7935-7949. <https://doi.org/10.1175/JCLI-D-19-0149.1>.
979
- 980 Simmonds, I., Keay, K. and Lim, E.-P. (2003) Synoptic Activity in the Seas around Antarctica. Monthly
981 Weather Review, 131(2), 272-288. [https://doi.org/10.1175/1520-0493\(2003\)131](https://doi.org/10.1175/1520-0493(2003)131<0272:SAITSA>2.0.CO;2)
982 [<0272:SAITSA>2.0.CO;2](https://doi.org/10.1175/1520-0493(2003)131<0272:SAITSA>2.0.CO;2)
983
- 983 Smith, B., Fricker, H. A., Gardner, A. S., Medley, B., Nilsson, J., Paolo, F. S., Holschuh, N., Adusumilli,
984 S., Brunt, K., Csatho, B., Harbeck, K., Markus, T., Neumann, T., Siegfried, M. R. and Zwally, H. J. (2020)
985 Pervasive ice sheet mass loss reflects competing ocean and atmosphere processes. Science, 368, 1239-1242.
986 <https://doi.org/10.1126/science.aaz5845>.
987
- 988 Speirs, J. C., McGowan, H. A., Steinhoff, D. F. and Bromwich, D. H. (2013) Regional climate variability
989 driven by foehn winds in the McMurdo Dry Valleys, Antarctica. International Journal of Climatology, 33,
990 945-958. <https://doi.org/10.1002/joc.3481>.
991
- 992 Speirs, J. C., Steinhoff, D. F., McGowan, H. A., Bromwich, D. H. and Monaghan, A. J. (2010) Foehn Winds
993 in the McMurdo Dry Valleys, Antarctica: The Origin of Extreme Warming Events. Journal of Climate,
994 23(13), 3577-3598. <https://doi.org/10.1175/2010JCLI3382.1>.
995
- 996 Stanton, T. P., Shaw, W. J., Truffer, M., Corr, H. F. J., Peters, L. E., Riverman, K. L., Bindschadler, R.,
997 Holland, D. M. and Anandakrishnan, S. (2013) Channelized Ice Melting in the Ocean Boundary Layer
998 Beneath Pine Island Glacier, Antarctica. Science, 341, 1236-1239.
999 <https://doi.org/10.1126/science.1239373>.
1000



- 1001 Steinley, D. (2006) K-means clustering: A half-century synthesis. *British Journal of Mathematical and*
1002 *Statistical Psychology*, 59, 1-34. <https://doi.org/10.1348/000711005X48266>.
- 1003
- 1004 Stigter, E. E., Litt, M., Steiner, J. F., Bonekamp, P. N. J., Shea, J. M., Bierkens, M. F. P. and Immerzeel,
1005 W. W. (2018) The Importance of Snow Sublimation on a Himalayan Glacier. *Frontiers in Earth Sciences*,
1006 6, 108. <https://doi.org/10.3389/feart.2018.00108>.
- 1007
- 1008 The IMBIE team (2018) Mass balance of the Antarctic Ice Sheet from 1992 to 2017. *Nature*, 558, 219-222.
1009 <https://doi.org/10.1038/s41586-018-0179-y>.
- 1010
- 1011 Tian, L., Li, H., Li, F., Li, X., Du, X. and Ye, X. (2018) Identification of key influence factors and an
1012 empirical formula for spring snowmelt-runoff: A case study in mid-temperate zone of northeast China.
1013 *Scientific Reports*, 8, 16950. <https://doi.org/10.1038/s41598-018-35282-x>.
- 1014
- 1015 Toyota, T., Massom, R., Tateyama, K., Tamura, T., Fraser, A. (2011) Properties of snow overlying the sea
1016 ice off East Antarctica in late winter, 2007. *Deep Sea Research Part II: Topical Studies in Oceanography*,
1017 58, 1137-1148. <https://doi.org/10.1016/j.dsr2.2010.12.002>.
- 1018
- 1019 Turner, J. (2004) The El Nino-Southern Oscillation and Antarctica. *International Journal of Climatology*,
1020 24, 1-31. <https://doi.org/10.1002/joc.965>.
- 1021
- 1022 Turner, J., Phillips, T., Hosking, J. S., Marshall, G. J. and Orr, A. (2013) The Amundsen Sea low.
1023 *International Journal of Climatology*, 33, 1818-1829. <https://doi.org/10.1002/joc.3558>.
- 1024
- 1025 van den Broeke, M. R. (1997) Spatial and temporal variation of sublimation on Antarctica: Results of a
1026 high-resolution general circulation model. *Journal of Geophysical Research*, 102, 29765-29777.
1027 <https://doi.org/10.1029/97JD01862>.
- 1028
- 1029 [Dataset] Vermote, E. (2015a) MOD09CMG MODIS Surface Reflectance Daily L3 Global 0.05Deg CMG.
1030 NASA EOSDIS Land Processes DAAC. <http://doi.org/10.5067/MODIS/mod09cmg.006>.
- 1031
- 1032 [Dataset] Vermote, E. (2015b) MYD09CMG MODIS Surface Reflectance Daily L3 Global 0.05Deg CMG.
1033 NASA EOSDIS Land Processes DAAC. <http://doi.org/10.5067/MODIS/myd09cmg.006>.
- 1034
- 1035 Webber, B. G. M., Heywood, K. J., Stevens, D. P., Dutrieux, P., Abrahamsen, E. P., Jenkins, A., Jacobs, S.
1036 S., Ha, H. K., Lee, S. H. and Kim, T. W. (2017) Mechanisms driving variability in the ocean forcing of
1037 Pine Island Glacier. *Nature Communications*, 8, 14507. <https://doi.org/10.1038/ncomms14507>.
- 1038
- 1039 Wiesenekker, J. M., Munneke, P. K., Van den Broeke, M. R. and Smeets, C. J. P. P. (2018) A Multidecadal
1040 Analysis of Fohn Winds over Larsen C Ice Shelf from a Combination of Observations and Modeling.
1041 *Atmosphere*, 9(5), 172. <https://doi.org/10.3390/atmos9050172>.
- 1042



- 1043 Willie, J. D., Favier, V., Dufour, A., Gorodetskaya, I. V., Turner, J., Agosta, C. and Codron, F. (2019) West
1044 Antarctic surface melt triggered by atmospheric rivers. *Nature Geosciences*, 12, 911-916.
1045 <https://doi.org/10.1038/s41561-019-0460-1>.
1046
- 1047 Willie, J. D., Favier, V., Gorodetskaya, I. V., Agosta, C., Kittel, C., Beeman, J. C., Jourdain, N. C., Lenaerts,
1048 J. T. M. and Codron, F. (2021) Antarctic atmospheric river climatology and precipitation impacts. *Journal*
1049 *of Geophysical Research: Atmospheres*, 126, e2020JD033788. <https://doi.org/10.1029/2020JD033788>.
1050
- 1051 Willie, J. D., Favier, V., Jourdain, N. C., Kittel, C., Turton, J. V., Agosta, C., Gorodetskaya, I. V., Picard,
1052 G., Codron, Santos, C. L.-D., Amory, C., Fettweis, X., Blanchet, J., Jomelli, V. and Berchet, A. (2022)
1053 Intense atmospheric rivers can weaken ice shelf stability at the Antarctic Peninsula. *Communications Earth*
1054 *& Environment*, 3, 90. <https://doi.org/10.1038/s43247-022-00422-9>.
1055
- 1056 Wingham, D. J., Wallis, D. W. and Shepherd, A. (2009) Spatial and temporal evolution of Pine Island
1057 Glacier thinning, 1995-2006. *Geophysical Research Letters*, 36, L17501.
1058 <https://doi.org/10.1029/2009GL039126>.
1059
- 1060 Yang, J., Yau, M. K., Fang, X., Pomeroy, J. W. (2010) A triple-moment blowing snow-atmospheric model
1061 and its application in computing the seasonal wintertime snow mass budget. *Hydrology and Earth System*
1062 *Sciences*, 14, 1063-1079. <https://doi.org/10.5194/hess-14-1063-2010>.
1063
- 1064 Yuan, X. (2004) ENSO-related impacts on Antarctic sea ice: a synthesis of phenomenon and mechanisms.
1065 *Antarctic Science*, 16(4), 415-425. <https://doi.org/10.1017/S0954102004002238>.
1066
- 1067 Yuan, X. and Martinson, D. G. (2001) The Antarctic dipole and its predictability. *Geophysical Research*
1068 *Letters*, 28, 3609-3612. <https://doi.org/10.1029/2001GL012969>.
1069
- 1070 Zhang, X., Wu, B. and Ding, S. (2022) Combined effects of La Nina events and Arctic tropospheric
1071 warming on the winter North Pacific storm track. *Climate Dynamics*. [https://doi.org/10.1007/s00382-022-](https://doi.org/10.1007/s00382-022-06389-9)
1072 [06389-9](https://doi.org/10.1007/s00382-022-06389-9).
- 1073 Zheng, M. and Li, X., (2022) Distinct patterns of monthly Southern Annular Mode events. *Atmospheric*
1074 *and Oceanic Science Letters*, 15, 100206. <https://doi.org/10.1016/j.aosl.2022.100206>.
- 1075 Zou, X., Bromwich, D. H., Montenegro, A., Wang, S.-H. and Bai, L. (2021a) Major surface melting over
1076 the Ross Ice Shelf part I: Foehn effect. *Quarterly Journal of the Royal Meteorological Society*, 147, 2874-
1077 2894. <https://doi.org/10.1002/qj.4104>.
1078
- 1079 Zou, X., Bromwich, D. H., Montenegro, A., Wang, S.-H. and Bai, L. (2021b) Major surface melting over
1080 the Ross Ice Shelf part II: Surface energy balance. *Quarterly Journal of the Royal Meteorological Society*,
1081 147, 2895-2916. <https://doi.org/10.1002/qj.4105>.
1082
- 1083 Zou, X., Bromwich, D. H., Nicholas, J. P., Montenegro, A. and Wang, S.-H. (2019) West Antarctic surface
1084 melt event of January 2016 facilitated by foehn warming. *Quarterly Journal of the Royal Meteorological*
1085 *Society*, 145, 687-784. <https://doi.org/10.1002/qj.3460>.